A FINITE ELEMENT MODEL FOR INVESTIGATION OF NUCLEAR STRESSES IN ARTERIAL ENDOTHELIAL CELLS

by

Charles B. Rumberger

A Thesis

Submitted to the Faculty of Purdue University

In Partial Fulfillment of the Requirements for the degree of

Master of Science in Biomedical Engineering

Department of Biomedical Engineering

Indianapolis, Indiana

December 2022

THE PURDUE UNIVERSITY GRADUATE SCHOOL
STATEMENT OF COMMITTEE APPROVAL

Dr. Julie Ji, Chair

Department of Biomedical Engineering

Dr. Hiroki Yokota

Department of Biomedical Engineering

Dr. Andres Tovar

Department of Mechanical and Energy Engineering

Approved by:

Dr. Joseph Wallace

To my former students at NPCA
and Sunday school students at Twin Valley FWB
who always inspired me to keep learning

ACKNOWLEDGMENTS

I would like to acknowledge Kevin Carr for his help with flow chamber construction; Robert Meagher for his assistance in resolving the frequent network and software issues encountered; former lab members Nathan Witt, Kirstie Queener, and Tamar Al-Muhtaseb for past work on this project and for taking their time to offer valuable insight for its further development; Dr. Khosrow Nematollahi, Dr. Andres Tovar, and Dr. Hiroki Yokota for their advice on certain questions related to the model; Dr. Julie Ji for her direction and guidance and for giving me the opportunity to join her lab to pursue this work; Adyota Gupta for being an experienced listener able to offer knowledgeable advice as a friend and peer; Sherry Clemens for keeping me accountable with academic deadlines and connecting me to resources; and Dr. Joseph Wallace and the Department of Biomedical Engineering at IUPUI for trusting me with this thesis opportunity. Most of all, I would like to acknowledge God who provided strength, purpose, and opportunity to pursue this work.

TABLE OF CONTENTS

LIST OF TABLES

LIST OF FIGURES

LIST OF ABBREVIATIONS

MTOC	microtubule organizing center
MT	microtubule
AF	actin filament
BAEC	bovine arterial endothelial cell
HAEC	human arterial endothelial cell
PAEC	porcine arterial endothelial cell
RAEC	rabbit arterial endothelial cell
HUVEC	human umbilical vein endothelial cell
NET	nuclear envelope transmembrane proteins
LINC	linker of nucleus to cytoskeleton
ECM	extracellular matrix
LDL	low-density lipoprotein
HDL	high-density lipoprotein
HGPS	Hutchinson-Gilford progeria syndrome
EDMD	Emery-Dreifuss muscular dystrophy
DCM	dilated cardiomyopathy
CMT	Charcot-Marie-Tooth disease
FPLD	familial partial lipodystrophy of Dunnigan type
AFM	atomic force microscopy

ABSTRACT

Cellular structural mechanics play a key role in homeostasis by transducing mechanical signals to regulate gene expression and by providing adaptive structural stability for the cell. The alteration of nuclear mechanics in various laminopathies and in natural aging can damage these key functions. Arterial endothelial cells appear to be especially vulnerable due to the importance of shear force mechanotransduction to structure and gene regulation as is made evident by the prominent role of atherosclerosis in Hutchinson-Gilford progeria syndrome (HGPS) and in natural aging. Computational models of cellular mechanics may provide a useful tool for exploring the structural hypothesis of laminopathy at the intracellular level. This thesis explores this topic by introducing the biological background of cellular mechanics and lamin proteins in arterial endothelial cells, investigating disease states related to aberrant lamin proteins, and exploring computational models of the cell structure. It then presents a finite element model designed specifically for investigation of nuclear shear forces in arterial endothelial cells. Model results demonstrate that changes in nuclear material properties consistent with those observed in progerin-expressing cells may result in substantial increases in stress concentrations on the nuclear membrane. This supports the hypothesis that progerin disrupts homeostatic regulation of gene expression in response to hemodynamic shear by altering the mechanical properties of the nucleus.

1. INTRODUCTION

1.1 Background Biology

The cardiovascular system is composed of the heart, arterial system, and venous system. Both arteries and veins are composed of three layers as illustrated in Figure 1.1. The outermost layer, the tunica adventitia or tunica externa, is the most rigid layer and is rich in fibroblasts and collagen. The middle layer, the tunica media, Is more elastic and is rich in smooth muscle cells and elastin. The innermost layer, the tunica intima, is the thinnest layer being composed of a monolayer of endothelial cells and the basement membrane to which these cells adhere.

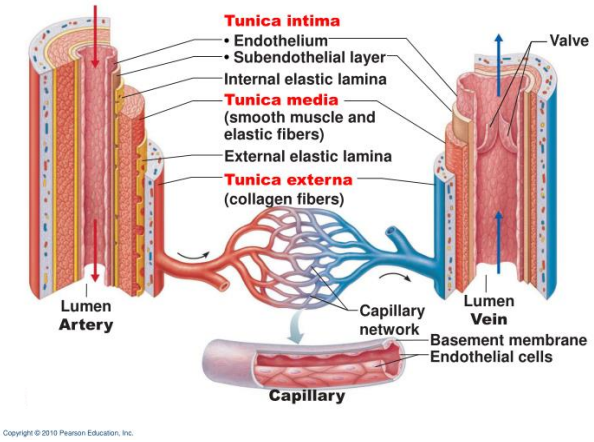

Figure 1.1. Blood Vessel Structure.

The arterial system carries blood away from the heart and is under higher pressure than the venous system. Arteries are characterized by a thicker vessel wall in general and a thicker tunica adventitia in particular than the venous system. This design is related to function as the arterial system must withstand higher pressure blood flow. This structural reinforcement is greatest is the descending aorta where the blood exits the left ventricle to supply the non-pulmonary organs of the body. The venous system, by contrast, carries low-pressure blood toward the heart. It also serves as a fluid reservoir for the cardiovascular system and, consistent with this function, is characterized by a thinner adventitia and thinner vessel thickness overall than the arterial system. Progressive hardening and narrowing of the blood vessels proceed predictably with age but may be strongly influenced by genetic factors, lifestyle factors, co-morbidities, and local vessel geometry. Atherosclerosis is largely a disease of the arterial system rather than the venous system.

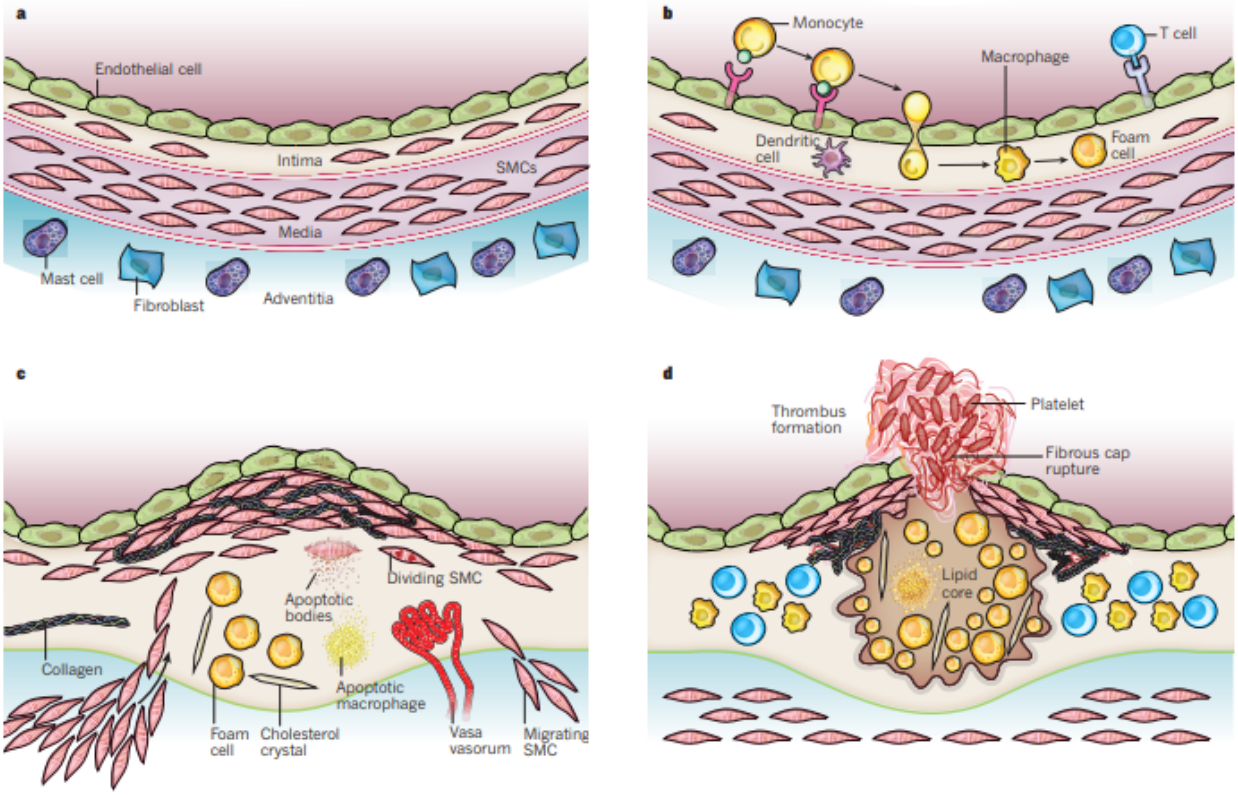

Figure 1.2. Progress of Atherosclerosis.
The vessel is initially in a healthy state with three arterial layers and an endothelial cell monolayer on the lumen side (a). Recruitment of leukocytes entering the tunica intima through diapedesis leads to foam cell formation (b). Plaque develops including smooth muscle cell migration, fiber generation, extracellular debris from macrophage apoptosis, and formation of cholesterol crystals (c). Thrombosis may occur leading to complications ranging from scarring and thickening of the vessel to complete arterial occlusion(d). [1]

1.1.1 Disease State: Atherosclerosis

Atherosclerosis is the leading cause of death in developed countries and is characterized by fibrotic lesions which restrict arterial blood flow [1], [2]. Lesions are characterized by migration of smooth muscle cells from the tunica media to the tunica intima arterial layer, excess ECM production in the vessel wall, extracellular lipids, inflammation, foam cells, and cholesterol crystals [1]. Atherosclerotic plaques tend to form preferentially at the outer wall of aortic bifurcations [2]. Research over the past few decades has identified low shear stress

and turbulent flow at these geometries as key contributors to atherogenesis [2]. In addition, endothelial cell turnover rate increases under low shear or disturbed flow conditions including increased endothelial cell proliferation and apoptosis [2]. There is strong evidence that such flow conditions contributes to the lack of tight junctions in the endothelial cell monolayer which is believed to be a key factor in allowing lipids to pass from the blood stream to accumulate in the vessel wall [2]. Experimental evidence that endothelial cells exhibit an atheroprotective biochemical and structural profile in response to shear stress has already been discussed. Further evidence has shown that transient or disturbed shear flow appears to lack this biochemically atheroprotective feedback mechanism resulting in unmitigated stress forces felt by the cell. This leads to random cell orientation, upregulated MCP-1, and JNK activation at sites of disturbed flow [3]. In addition to geometric considerations, atherosclerosis risk and lesion severity is known to increase with age, even in healthy individuals. Although this is likely due in large part to the cumulative nature of atherosclerotic lesions, cellular aging of the endothelial cells presents another likely contributor. Changes in the arterial ECM including decreased elastin content and increased collagen crosslinking contribute to arterial stiffness in aged individuals, significantly contributing to cardiovascular disease [4]. Epigenetic factors and lamin A/C mutations are also likely contributors to vascular aging as will be discussed further in the following section [5].

There are some clinical interventions which help to reduce the risk in vulnerable patient populations though many therapeutic targets remain elusive. Low-density lipoprotein (LDL) is associated with plaque formation. Treatment of high-risk patients with statins, a class of drugs that inhibits part of the LDL pathway, greatly improves prognosis [1]. There remains, however, progress to be made in targeting LDL for plaque reduction. High-density lipoprotein (HDL) and certain triglycerides are associated with good cardiovascular health. Various drugs aimed at increasing HDL or triglyceride levels, however, have not yet been clearly shown to effectively reduce cardiovascular incidents [1]. Anti-oxidants could in theory reduce oxidative stress associated with atherogenesis, but experimental results remain inconclusive. Some of the difficulties in crafting effecting therapeutic agents may have to do with the biological differences between humans and the mice which are used as a model organism for drug evaluation [1].

1.1.2 Response to Mechancial Stimulation

Cellular mechanotransduction is the process whereby a force stimulus is transmitted from the extracellular environment to the interior of the cell to trigger some kind of biological response. A familiar example of this is the transduction of air pressure waves into an action potential by the cells of the inner ear enabling the perception of sound. No less important is the mechanotransduction of shear stress exerted by blood flow and circumferential stretch from arterial compliance on arterial endothelial cells for the proper regulation of healthy arteries.

1.1.3 Biochemical Response

Arterial endothelial cells form a monolayer lining the lumen of arteries and thus are exposed to shear forces exerted by blood flow through the arterial lumen. This mechanical stimulus produces both chemical and structural responses within the endothelial cell based primarily on the degree of shear. The shear force experienced by the endothelial cell is dependent both on blood flow and on the geometry of the vessel at the location of the cell. Although extremely high flow conditions may cause damage to endothelial cells [6], flow rates within the realm of physiological relevance (between 10-70 $\frac{dynes}{cm^2}$ in the arterial network) favor an atheroprotective biochemical signature compared to low flow or static conditions [2]. High hemodynamic stresses promote the production of vasodilators such as nitric oxide and prostacyclin, antioxidant enzymes such as cyclooxygenases and superoxide dismutases, growth regulator TGF-, and the fibrolytic factor tissue-type plasminogen acti-

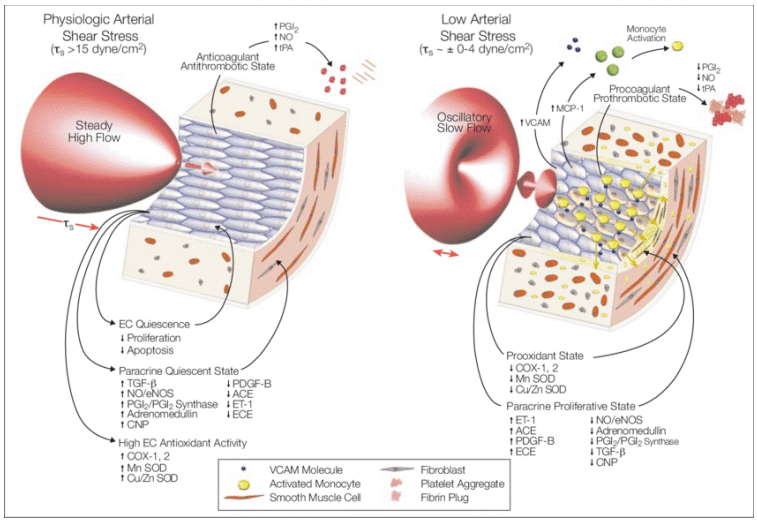

Figure 1.3. HAEC response to shear stress. [2]

vator [2]. Low shear stress conditions, on the other hand, result in decreased expression of the aforementioned factors and increased expression of vasoconstrictors, growth factors PDGF-A and PDGF-B, inflammatory mediator MCP-1, and adhesion molecule VCAM-1 [2]. In addition, low shear stress conditions have been reported to increase the rate of endothelial cell turnover including both increased proliferation and apoptosis [2]. Cell response to changes in mechanical stress appears to include the time-dependent activation of Rho and Ras intracellular signaling pathways [3]. Together, these chemical signals are designed to produce an atheroprotective endothelial cellular response to shear stress as a feedback loop designed to minimize stress forces on the cell. The continuous activation of this feedback loop causes geometric reorientation of the cell cytoskeleton and overall structure via Rho signal pathway activation, downregulation of the pro-inflammatory MCP-1 protein, upregulation of the anti-proliferation KLF2 protein, and decreased activation of the pro-apoptotic JNK signal pathway [3].

1.1.4 Structural Response

In addition to chemical changes, endothelial cells undergo mechanical changes in response to shear stress. Under steady flow conditions, cells become stiffer, cell-cell junctions become tighter, and both cells and cell fibers become elongated in the direction of flow (see Fig. 1.4) [7], [8]. The actin cortex of the cell thickens while the actin filaments of the cell become aligned roughly in the direction of blood flow. The aspect ratios of both the cell as a whole and of the nucleus become altered to favor a thinner, shorter, more elongated structure. Although the literature is not in clear agreement, it has been suggested that endothelial cell response to the onset of shear flow takes place in three phases based on flow chamber experiments with BAECs [8]. In the first stage (0-3 hours) the nucleus migrates

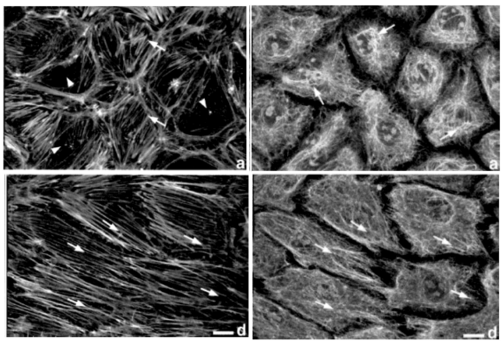

Figure 1.4. Actin realignment. Actin filaments (left) and intermediate filaments (right) before (a) and after (d) 24 hours exposure to high shear flow [7]

toward the downstream portion of the cell, basal stress fibers increase in number, and adhesion sites move to periphery of the cell base. During the second phase (3-6 hours) the MTOC and the nucleus shift to the upstream side of the cell and characteristics of motility appear. In the final stage (12-24 hours) numerous changes are said to take place. The cells elongate parallel to flow, gaps between cells close, the cell base thickens, cell shape becomes more ellipsoidal, intercellular adhesions increase, and the MTOC nucleus resume random orientations [8].

1.1.5 Cell Polarization

Cell polarization may be observed by the position of the cell nucleus relative to other cellular components such as the MTOC. Both in vivo and in vitro experiments have attempted to determine the relationship between the direction of blood flow and the direction of cell polarization. A 2006 study by McCue et al. found that cell polarity as evidenced by the position of the MTOC relative to the nucleus was dependent on shear stress, vessel type, and age [9]. Changes in polarity were mediated by microfilament reorganization and were regulated by GSK-3B as determined by experiments blocking microtubule assembly or disassembly and by microinjection of GSK-3B [9]. In vitro, cell reorganization was blocked by either destabilization (nocodazole) or hyperstabilization (taxol) of microtubules [9]. This indicates that structural reorganization in response to mechanical stimuli depends on biochemical mediation. Accompanying In vivo experimentation created a stenosis and observed that endothelial cells in the disturbed flow region of stenosis lost or possibly reversed their polarity [9]. Previous work had considered polarity to be cardio-centric (upstream in arteries and downstream in veins), but this study concluded that polarity depends on the direction of shear flow. Specifically, MTOCs were observed to align downstream of the nucleus after 24 hours of 15 $\frac{dynes}{cm^2}$ shear flow using PAECs in a parallel plate flow chamber [1]. This orientation is in agreement with the findings of a 2003 study which identified Cdc42 activation as a mediator in this structural change [10]. In terms of progression, new focal adhesions appear to lead to Cdc42 activation which initiates MTOC migration, resulting in actin reorientation [10]. This finding regarding cell polarization, however, appears to contradict the previously

discussed findings of Galbraith et al. which reported that the MTOC moves upstream of the nucleus after 1.5 hours of shear flow in an experiment using BAECs under 15.2 $\frac{dynes}{cm^2}$ flow before resuming a random orientation within 24 hours [7]. On the contrary, a 2013 study by Ginsberg et al. found that HUVECs polarize with the MTOC upstream of the nucleus, attributing this effect largely to drag forces exerted on the cell nuclei which bulge up above the layer of confluency [11]. To further complicate the question, the in vivo portion of the McCue et al. study observed that polarity in rabbit abdominal aortas changes between upstream and downstream configurations depending on age [9]. These differences may be in part explained by a 2001 publication by Gundersen et al. which reported that the MTOC migrates toward the leading edge of a migrating cell and that this migration was dependent on Cdc42 activation, but not on Cdc42-mediated actin restructuring [12]. While this opens the possibility that cell polarization may be sensitive to any local variations affecting cell migration, the applicability of the results may be limited by the fact that 3T3 fibroblasts rather than endothelial cells were used in the Gundersen et al. study. The scenario seems plausible, however, in light of the finding of Ginsberg et al. that polarization was affected by confluency [11].

1.1.6 Wound Healing

Endothelial cell response to mechanical stimulation also has implications for wound healing and cell motility. A 2005 study by Andrea Gojova and Abdul Barakat using BAECs examined endothelial wound closure relative to flow-induced shear stress and membrane stiffness [13]. Wounds were created by scratching the cell monolayer perpendicular to the direction of flow in a flow chamber. Observations were taken under static, low shear, and high shear conditions for up to 24 hours following monolayer disruption. High shear led to more rapid closure than low shear with greater cell migration at the upstream edge than at the downstream edge of the wound [13]. Net wound closure speed was found to be similar between static and high shear stress (19 $\frac{dynes}{cm^2}$) but was significantly retarded under low shear stress (3 $\frac{dynes}{cm^2}$) [13]. This is not entirely in agreement with previous publications suggesting that high shear stress speeds wound closure [2]. Cell membrane stiffening was found to slow

cell migration and wound closure but decreasing cell stiffness below native levels was not found to have any significant effect [13]. It should be noted, however, that the method of cell stiffening was by incorporation of additional cholesterol into the cell membrane which may not mimic the mechanisms underlying membrane stiffness regulation in vivo.

1.1.7 Arterial Endothelial Cells

The mechanical structure of the cell depends on cytoskeletal, nuclear, and extracellular components. Fibrous elements of the cytoskeleton include microtubules, F-actin filaments, and intermediate filaments. Microtubules extend from a common body called the microtubule organizing center (MTOC). Although individual microtubules are approximately 25 nm in diameter, multiple microtubules are often joined to form bundles of with variable non-linear mechanical properties [9], [14]. Actin filaments are only 4-7 nm in diameter but form branched networks that both provide tensile strength to the cell and serve a primary role in cell locomotion. They also create a network geometry with microtubules, greatly reinforcing the compressive strength of the overall structure [15]. A dense network of actin filaments provides structural support at the inner surface of the cell membrane, forming a body known as the actin cortex. This body plays a primary role in controlling the structural characteristics and overall shape of the cell and may be from 100 to 1000 nm in thickness. Intermediate filaments represent a family of various protein structures of about 10 nm diameter. In particular, soft keratin types I and II intermediate filaments are significantly present in the cytoskeleton of endothelial cells. In addition to their structural roles, actin-microtubule interaction is important in organelle movement within the cytoplasm [16]. All three of these filamentous cytoskeletal structures are dynamically regulated to allow rapid restructuring in response to mechanical signals or to participate in cell motility.

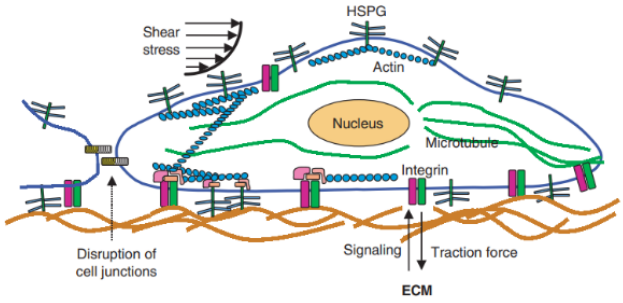

Figure 1.5. Endothelial cell diagram. [8]

Integrin proteins anchor actin filaments within the cell membrane and to the external environment through external connections to extracellular matrix (ECM) and neighboring cells (Fig. 1). The cell-cell junctions are of great importance in maintaining the impermeability of the endothelial monolayer. In the case of arterial endothelial cells, the ECM component is basement membrane rich in heparin. The lumen side of the cell is covered with glycoproteins that make us a glycocalyx layer ranging in thickness from approximately 50 nm in arteries to 1000 nm in capillaries [17]. This layer may behave as a force buffer [17].

The cell nucleus also has a structural system. The inner and outer nuclear membranes are separated by a space of 100 nm but connected through nuclear pore complexes [18]. The inner nuclear membrane is characterized by the presence of nuclear envelope transmembrane proteins (NETs) while the outer nuclear envelope is continuous with the endoplasmic reticulum [18]. The nuclear envelope is also connected to the cytoskeleton through linker of nucleus to cytoskeleton (LINC) protein complexes [19]. The nucleoskeleton itself is composed of various proteins classified as intermediate filaments. Lamin A/C, a type V intermediate filament, plays a key role in nuclear mechanics by forming the primary structural protein of the nuclear envelope [18].

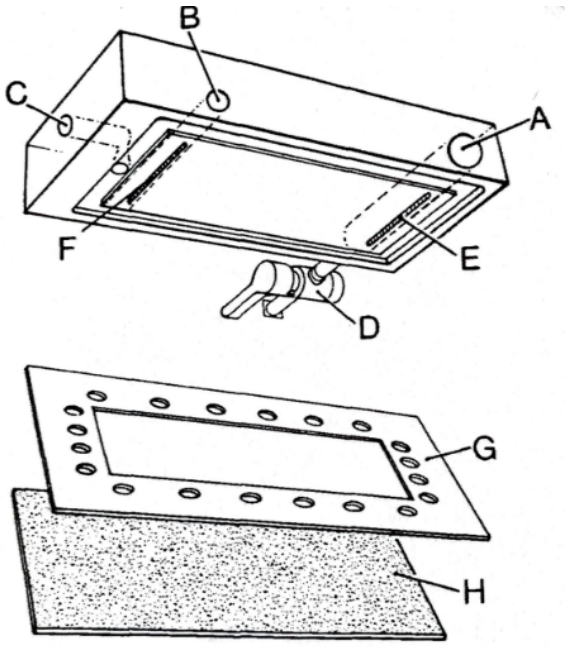

Figure 1.6. Flow chamber diagram. In the original design, the glass slide (H) is secured by a vacuum (C) and gasket (G). Flow enters the chamber (A) and passes through entry slit (E) before exiting via exit slit (F) and flow outlet (B). A bleeder valve allows release of trapped air (D). [6]

1.1.8 Experimental Methods

Understanding the state of knowledge regarding endothelial cell regulation requires some knowledge of commonly used experimental methods. In vitro experiments commonly make

use of various cell types including human arterial endothelial cells (HAECs) [20], bovine arterial endothelial cells (BAECs) [13], porcine endothelial cells (PAECs) [9], and human umbilical vein endothelial cells (HUVECs) [19]. In order to simulate the effect of blood flow, cells may be cultured in a parallel plate flow chamber. In the simplest form of this setup, a pressure differential is maintained to drive constant flow of cell growth media through a slit at one end of the cell culture chamber with an exit slit at the opposite end of the chamber (see Fig. **??**) [6]. Although a broader range of values shear flow stresses may be acceptable [6], shear flow experiments frequently define high shear or physiological shear between 12-19 $\frac{dynes}{cm^2}$ [3], [7], [9], [10], [13]. Flow chambers may be modified to simulate various physiological or pathological conditions including low flow, pulsatile flow, or reciprocating flow conditions through fluid pressure controls or disturbed flow conditions using modified flow chamber geometries [3]. One application of flow chamber experiments is wound closure. This type of experiment cultures endothelial cells to confluence before making a clean scratch that disrupts the continuity of the endothelial cell monolayer with the goal of observing cell migration characteristics relative to flow conditions [13]. In addition to flow chambers, apparatuses to simulate cyclic stretch are commonly used for in vitro studies to mimic the motion of the arterial wall due to vessel compliance [3].

Cells in a parallel plate flow chamber are subject to shear stress. Shear stress is the tangential stress experienced by the cells due to fluid flow and can be expressed mathematically as

$$\tau = \frac{6Q\mu}{bh^2}$$

where is shear stress, Q is fluid flow rate, b is the width of the inlet slit, h is the height of the flow channel, and is the viscosity of the fluid (cell culture media) [6].

Additional physiological mechanical stimuli which may be examined in vitro include normal stress due to pulsatile flow and vessel compliance and cyclic biaxial strain due to circumferential and longitudinal stretch of the vessel wall. In vivo experiments have also been used to gain a better understanding of arterial endothelial cell function and of pathologies associated with lamin mutations. Such experiments may investigate the role of specific genetic alterations in animals [5], drug interventions [1], or of surgical operations which alter

arterial geometry [9]. Care must be taken in interpreting the results of animal studies since existing animal models may recapitulate only certain aspects of human disease states such that findings may or may not be translatable [1], [18], [21]. Studies using aggregate patient data or histological studies may also provide useful insights.

1.1.9 Lamins

Lamins are a class of protein which plays a key role in nuclear mechanics of cells throughout the body. This protein family contains Lamins A, B, and C which range in size between 65-75 kDa and are classified as type V intermediate filament proteins [18]. The amino head is connected to a carboxyl tail through a series of four coiled-coil domains which collectively form an alpha helix structure [18]. Lamins A/C result from alternative splicings encoded on chromosome 1q21.1-21.3 while B-type lamins are encoded on chromosome 5q23.3-q31.1 (LMNB1) or 19p13.3 (LMNB2) [18]. B-type lamins are necessary for survival and are likely the primary structural proteins of the nuclear lamina [18]. Complete loss of function in lamin A in humans results in fatality before or shortly after birth, but LMNA -/- mice may survive up to 8 weeks. Cell culture lines may also survive without functional lamin A [18]. Mutations in type A/C lamins are, however, responsible for the disease states observed in various laminopathies [18], [22]. Lamin plays a primary structural role in the nucleus and also links nuclear pores, determining the spacing of nuclear pores and other nuclear membrane integrated proteins. Lamins also impact both gene expression through their interactions with nuclear proteins and cytoskeletal organization through their interactions with cytosolic proteins [18]. Lamin A/C in particular appears to play a key role as a scaffolding protein involved in the organization of DNA within the nucleus [22].

Disease States: Laminopathies

Mutations to lamin A/C are implicated in a number of rare disorders, some affecting only particular tissues (muscle, peripheral nerves, or adipose tissue) and others causing systemic affects. Several of these laminopathies result in aged phenotypes, particularly in the case of Hutchinson-Gilford progeria [18]. Hutchinson-Gilford progeria syndrome (HGPS) is a rare

condition usually caused by a de novo C →T mutation in exon 11 of the lamin A/C gene located on chromosome 1 [21]. Although this still results in a glycine amino acid during translation, this mutation causes a gain of function which exposes a cryptic splice donor site important in post-translational modification [21], [23]. This splice site is 50 amino acids upstream of the natural splice site [18], [21]. The resulting truncated protein, progerin, lacks the recognition site for the protease ZMPSTE24 and therefore retains a farnesylated form left over from a previous stage of post-translational modification [21]. Possible mechanisms for disease progression of HGPS are discussed below, but the end result of this process is accelerated aging with death from cardiovascular failure usually occurring in early adolescence. Other laminopathies include Emery-Dreifuss muscular dystrophy (EDMD), dilated cardiomyopathy (DCM), Charcot-Marie-Tooth disease (CMT), familial partial lipodystrophy of Dunnigan type (FPLD), and atypical Werners syndrome. Drug development is likely the key clinical application of laminopathy studies.

Mechanistic Hypotheses of Laminopathies

At least four possible mechanisms have been proposed for linking lamin A/C mutations to clinical symptoms. These are the structural hypothesis, the gene expression hypothesis, the cell proliferation theory, and prelamin A (progerin) toxicity [18]. These four mechanisms are not mutually exclusive, and a significant body of evidence exists for each [18]. According to the structural hypothesis, nuclear fragility results from aberrant lamina leading to structural deformation and necrosis [5]. The gene expression hypothesis posits that lamin plays a direct or indirect role in DNA transcription [5], [22] while the cell proliferation theory proposes that defective lamin promotes rapid cell turnover (proliferation and apoptosis) leading to premature stem cell depletion and cellular senescence [18]. As its name suggests, the progerin toxicity hypothesis holds that progerin has a toxic effect in certain cells leading to pathological effects [18].

The structural and gene expression hypotheses in particular warrant further discussion. A few mechanistic pathways involved in the gene expression hypothesis of laminopathy stand out as likely candidates. Broadly speaking, nuclear envelope proteins appear to have an

effect on four signaling pathways: MAPK, Wnt-B-catenin, TGF-B, and Notch [22]. These pathways may well be affected by alterations in lamin protein structure. In addition, pocket proteins such as pRb are involved in many signaling pathways and appear to be regulated by lamin A/C and LAP2-a [22]. Intriguingly, altered epigenetic modifications have also been observed as a hallmark of HGPS and may well be involved in lamin-related diseases [22], [23].

One method of investigating these hypotheses involves the use of lamin-deficient cells. One such study using Lmna -/- mouse fibroblasts observed that the altered cells showed both decreased cytoskeletal stiffness and decreased nuclear stiffness [5]. Under cyclic strain, these cells showed increased nuclear deformation compared to controls [5]. Nuclear fragility and a 3-5% increase in incidents of nuclear rupture under applied strain was also observed. In addition to the evidence these findings provide for the structural hypothesis, it was found that the Lmna knockout cells showed impaired activation of mechanosensitive genes egr-1 and iex-1 and impaired cytokine-responsive gene activation [5].

The progerin hypothesis may also be examined using cell culture. One such study using multiple cell types including HeLa cells, osteosarcoma cells (Saos2), cells expressing an HGPS-like mutation, and HUVECs were evaluated to observe the effects of progerin accumulation on cell structure and function [19]. It was found that progerin-expressing cells showed reduced chromatin condensation, reduced force transduction to the nucleus, and greatly increased nuclear stiffness (9kPa compared to 4kPa controls) [19]. This last point may appear to contradict the results of the Lammerding et al. study which reported reduced nuclear stiffness Lmna -/- cells. The difference may be explained by the fact that one study used Lamin deficient cells while the other used cells expressing progerin to mimic laminopathic conditions. However, the result may be due to different responses by different nuclear components. Specifically, the Booth et al. study reported that progerin-expressing cells had a decrease in stiffness of the nuclear interior but an increased stiffness of the nucleoskeleton resulting in a net increase in the stiffness of the nucleus as a whole [19].

Vascular Disease in HGPS and Natural Aging

Although mutation in lamin A/C causes symptoms of premature aging, however, it is not immediately clear whether the reverse is true, i.e. whether aged individuals demonstrate accumulation of sporadic mutations to lamin-encoding genes. Furthermore, it appears that in Werners syndrome, mutated lamina is implicated only in atypical cases [18]. This raises the question of whether laminopathies necessarily play a role in aging or whether they simply mimic an aged phenotype. It has, however, been suggested that HGPS may serve as a model to better understand wild type vascular aging [24]. This suggestion is made more compelling by the fact that the cause of death for HGPS patients is almost invariably cardiovascular failure related to the arterial system [25]. Although some differences appear, fundamental similarities such as arterial occlusion, excessive collagen crosslinking, decreased smooth muscle cell populations, fibrotic lesions, and development of subintimal plaques appear in the cardiovascular disease phenotype of both HGPS and of aged individuals [25]. Further observations of mechanical stiffening, nuclear morphology changes, and epigenetic alterations in the endothelial cells in both conditions further suggest the possibility of a mechanistic link between the two disease states [4], [19], [23].

Phenotypical similarities between laminopathies such as HGPS and natural aging suggest the possibility of similar disease mechanisms. The progression of cardiovascular disease in HGPS and aging in particular raises the question of lamin A/C role in natural aging. To help answer this question, a 2010 histological study compared vascular tissues in two deceased HGPS patients with tissues found in 40 non-HPGS individuals of varying ages focusing especially on those of advanced age in the comparison [25]. Similarities in lesions including arterial occlusion, fibrosis, cholesterol crystals, and foam cells suggest the likelihood of similar mechanisms of vascular pathology in both HGPS and normal aging. Excess fibrosis in the tunica adventitia was noted in HGPS vs. aged non-HGPS tissues. Increased collagen and proteoglycan production was observed surrounding progerin-positive fibroblasts. Interestingly, although progerin was reported as increasing by an average of 3.4% throughout life in non-HGPS arterial walls, the lack of progerin in many individual older patients, the large standard deviation in progerin content at all ages, and the small progerin-positive cells in

even the most extreme cases (<100%) of aged non-HGPS patients [25] tend to undermine the idea that accumulated progerin is the primary driver of arterial aging. This is compared to HGPS patients who, despite similar lesions, had progerin levels 75% in cells of the arterial wall [25]. It should be noted that the idea of progerin accumulation as a driver of natural vascular tissue aging persists in research literature [24].

The question of mechanistic similarities between HGPS and natural aging was also addressed from a gene expression perspective by researchers at the National Cancer Institute. This 2006 study looked at epigenetic modifications and LMNA cryptic splicing rates in cell lines from young donors, old donors, and HGPS patients [23]. Sporadic LMNA cryptic site splicing in non-HGPS individuals showed no increase with age as measured by mRNA activity. Furthermore, progerin did not accumulate with age, consistent with the chart data, if not the interpretation, presented by Olive et al. Epigenetic modifications including decreased Tri-Me-K9H3 and HP1 nuclear presence were strongly correlated with age and with HGPS. LMNA also ceased to be detected in the nucleoplasm of aged individuals and in HGPS, being instead restricted to the nuclear envelope [23]. These changes occurred more rapidly in cell lines from aged donors. Negative phenotypic effects on cells were reversible upon inhibition of the cryptic splice site using Exo11. Concurrent with phenotypic recovery, Tri-Me-K9H3 and cell proliferation rates were restored to a more youthful cell state [23]. Taken together with the histological study performed by Olive et al., these results may suggest an accumulation of effects due to sporadic progerin production throughout a persons lifespan though progerin itself may not accumulate to reach very high levels. It should be noted that this idea may be somewhat controversial [24]. The Scaffidi-Misteli study goes on to speculate that the p53 checkpoint could induce senescence in cells with progerin-induced nuclear changes [23]. If true, this could mechanistically tie together the laminopathy, epigenetic, and cell senescence theories of aging. The mediator of progerin-induced damage in the absence of progerin accumulation, however, remains uncertain.

Altered cellular mechanics has been consistently identified as a feature of cardiovascular disease both in HGPS and in natural aging [4], [5], [19]. This is not surprising in the case of HGPS since a mutation is present in a gene for a key structural protein of the nuclear envelope. As discussed above, epigenetic alterations and progerin expression may provide other

mechanistic links joining both HGPS and normal aging to altered mechanics of the arterial endothelial cell [4], [23]. The key role of shear stress in maintaining an atheroprotective biochemical and structural profile makes these alterations of particular interest in the study of vascular disease progression since changing the mechanical properties of the intracellular components would reasonably be expected to interfere with the transduction of shear force signals to the cell nucleus for regulation of cell structure and cell signaling. Further study of mechanotransduction under the altered structural conditions imposed by HGPS or aging on endothelial cell biology could help to clarify the role of such changes in arterial disease.

1.2 Computational Methods

Many different approaches have been taken to mimic cell mechanical structure for the purpose of mechanical simulation. Although broadly composed of microtubules, actin filaments, and intermediate filaments, the cell cytoskeleton is far too complex in terms of its geometry, variance in elemental material properties, and total number of units to be modeled exactly. It is therefore necessary to make simplifying assumptions in order to limit the number and properties of materials involved in the simulation. These simplifying assumptions take many forms, but attempts have been made to categorize them broadly. One such method of categorization is to classify mechanical models of cells into continuum models, microstructural models, and hybrid models [26], [27]. This classification scheme, though useful, is somewhat arbitrary such that a great deal of variation may be found within a single category. Continuum models may, for example, define the cell interior as a homogenous material approximating the net mechanical behavior of the cell [26], [27], as a continuous spring network [28], or as adjoining layers with internally homogenous properties [29]. Tensegrity models, on the other hand, model the cytoskeletal network as a 3D truss composed of compression-only and tension-only elements assembled into a tensegrity structure. Hybrid models attempt to combine these two approaches by embedding a microstructure in a viscous medium [27]. It should be noted that, while tension elements may be presented as analogous to actin fibers and compression elements as analogous to microtubules, there is not a direct biological correspondence.

1.2.1 Finite Element Analysis Methods

The finite element method of structural analysis has been long and widely used in many engineering disciplines. This method of analysis has been applied to biomechanical structure in recent decades, allowing accurate and detailed prediction of local and global responses to applied loads by biological structures. The theory behind finite element analysis is has been widely discussed elsewhere and is an essential tool generally used across engineering fields. It is relevant to this discussion, however, to point out that the finite element workflow is generally divided into preprocessing, solving, and postprocessing stages and that the tasks involved in this workflow may be handled by a single software system or by multiple software systems working together. The preprocessing method includes defining geometry, defining material properties, meshing the geometry, and defining nodes and boundary conditions. Numerous software systems have been used to produce the cellular mechanical simulations here discussed including commercial, open-source, and custom-built computational tools. Software components may include such products as ANSYS [26], [30], MATLAB [27], Abaqus [27], or ADINA [29].

1.2.2 Hybrid Models

A number of very simple hybrid models have been proposed. One such model was published by researchers at the Brno University of Technology in the Czech Republic in 2021 [30]. This model stretches the definition of the hybrid model by incorporating beam elements and truss elements into the same model, thus creating a more complex structure than a true tensegrity model for representing the cytoskeletal components of the cell. This model uses 12 beam elements to represent microtubules, 36 tension-only prestressed truss links to represent actin filaments, and 24 pre-strained tension-only truss links to represent intermediate filaments [30]. Several geometric variations were presented in this model including spherical, truncated spherical, flat hexagonal, and domed hexagonal cell shapes. Another interesting model was put forward by Lloyd Chua, an engineering student at the University of Edinburgh in 2014. This model implemented an algorithm to define the number of tensegrity elements based on a cell input diameter [27]. Like the Jakka-Bursa model, only

regular geometric cell shapes were modeled, but unlike the Jakka-Bursa model, no MTOC is represented in the tensegrity structure geometry, nor are beam elements incorporated into the model [27]. In 2004, researchers at Trinity College in Dublin, Ireland put forward a hybrid model with a regular cell geometry based on the observed shape of a spreading chick fibroblast. The tensegrity portion of the model was composed of 6 compression struts to represent microtubules and 24 tension struts to collectively represent actin filaments and intermediate filaments [26]. The Chua model was in part based on the Prendergast-McGarry model. Neither model attempted to mimic the MTOC geometry and both retained a true tensegrity design using truss elements only [26].

The Prendergast model found that prestress was of primary importance in modelling flexural rigidity. The choice of Poissons ratio for modelling the compressibility of the cytoplasm was also found to greatly influence analysis results [26]. The Jakka-Bursa model revealed that tensegrity elements were far more important to cell stiffness under tension than under compression. Regarding cytoskeletal components, truss elements modeled on actin fibers were found to make the greatest contribution to cell stiffness under compression while microtubules made the greatest contribution under tension and intermediate filaments played very little role in either loading scenario in the model [30].

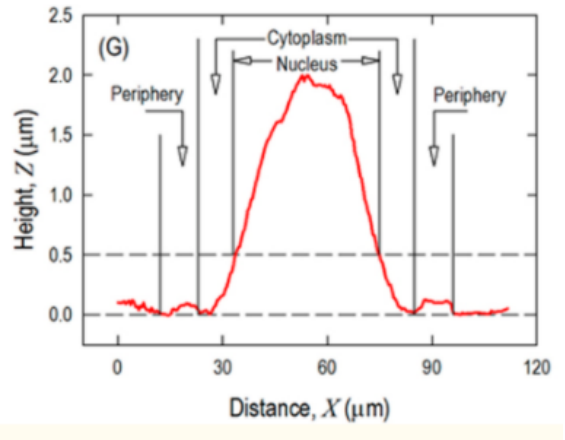

Figure 1.7. Endothelial cell profile [20] as measured by atomic force microscopy.

1.2.3 Limitations of Existing Models

There were a number of clear limitations to the models described for the purpose of endothelial cell study. Firstly, these models do not model the same cell types. The Jakka-Bursa model attempted to model a vascular endothelial cell. The Prendergast model, however, attempted to mimic the external geometry of a chick fibroblast while the Chua model

attempted to model a generic cell. The latter models examined structural loads designed to mimic atomic force microscopy (AFM) tests while the former simulation used compression and shear loads based on the in vivo environment of the vascular endothelial cell. None of the hybrid models discussed in this section appear to implement a shape that realistically approximates that of an arterial endothelial cell under shear stress. The number of tensegrity structure elements was relatively small in all three models and each model employed a regular geometric shape for the cell exterior with a nucleus embedded within the cell interior. This is very different from biological expectations regarding endothelial cells which could be more accurately modeled using irregular or elongated cell geometries with a significantly raised nucleus [17]. The latter point of concern is likely to be especially important in understanding cellular mechanics of endothelial cells since some forces may be transmitted to the nucleus more or less directly [11]. This is significant enough that a mathematical model produced by researchers at the University of Cambridge in 2000 considered it justifiable to ignore the cytoskeletal elements entirely, modeling the vascular endothelial cell as a raised nucleus instead [17]. By computing the total force on the raised nucleus at various orientations and geometries, it was found that total force is minimized when the major axis of the nucleus aligns with flow direction, the length-to-width ratio is approximately 2.2, and the height-to-width ratio is approximately 0.38 [17]. These values aligned closely with the experimentally observed aspect ratios, 2.23 and 0.27 respectively, in living endothelial cells as reported by an earlier study. It therefore appears likely that the shape and orientation of the endothelial cell nucleus under flow conditions is determined by a force reduction mechanism [17]. Furthermore, the geometric concept of a prominent raised nucleus under a stretched cell membrane agrees closely with observed AFM measurements of endothelial cell surface (see Fig. 5) [20].

Some important differences between the models in choice of mechanical properties and in experimental results are also instructive. Table 1 below compares several of the design parameters present in each of the three hybrid models discussed above. Numerical values represent elastic modulus for actin filaments (AFs), microtubules (MTs), nucleus, cytoplasm, and cell membrane together with the actin cortex. Not displayed are actin filaments which are assigned a Youngs modulus of 2.0 GPa by the Jakka-Bursa model. More model details

may be found in the individual model publications cited. Although each model justifies some or all modulus values with literature references, these values may be controversial. Various literature references place nuclear stiffness at 4kPa [19], intermediate filament stiffness at 0.9 GPa [31], and microtubule stiffness within a range of 0.1 to 7 GPa [14]. Differences in literature values may be due in part to the varying methods of experimental measurement, varying cell sources, and the the difficulty or impossibility of isolating and testing individual fibers. A more fundamental cause, however, is the non-linear behavior of these materials which are better described using stress-strain curves than with a linear elastic modulus [32]. In addition, the meaning of individual fiber properties may be of little use compared to the emergent mechanical properties of crosslinked fiber networks [31]. Furthermore, the extreme differences in structural geometry and number of elements between real and modeled cytoskeletal structures means that model elements are not necessarily best represented using identical properties to their analogous counterparts.

Table 1.1. Comparison of Select Published Hybrid Models.

Model	**AFs (GPa)**	**MTs (GPa)**	**Nucleus (kPa)**	**Cytoplasm (kPa)**
Prendergast	2.6	1.2	0.4	0.1
Jakka-Bursa	2.2	1.2	5	0.5
Chua	1.7	6.5E5	2.5	0.25
Model	**Membrane/ Cortex (kPa)**	**N truss elements**	**Shape**	**Software**
Prendergast	1.0	30	truncated sphere	ANSYS
Jakka-Bursa	2.0	72	hexagonal prism	ANSYS
Chua	5500	user-defined	truncated sphere	Abaqus

1.3 Conclusions

Endothelial cell structural components serve as a key mediator in the maintenance of a healthy arterial system through their role in transducing mechanical stimulation to help regulate gene expression. This system in known to fail in predictable ways that are phenotyp-

ically similar in natural aging and in progeria resulting from mutations affecting A/C type lamins. Despite progress in understanding the mechanisms involved, many questions remain. Some of these questions may not be answerable through cell culture or animal studies and access to the resources necessary to perform such studies is limited. Finite element models of intracellular structural mechanics may therefore be a useful tool in the future of research surrounding arterial aging and laminopathies. Numerous models have been developed to accomplish this goal, laying the foundation of future development. Additional refinement, however, is needed to advance such computations models to reach their full potential as tools in this field of research.

One question that may be addressed using computational models of endothelial cellular mechanics include that of cell polarity in response to flow. This includes MTOC and nuclear position relative to the direction of flow. Conflicting results appear within existing research. Mechanical modelling could give insight regarding the distribution of forces within the cell when exposed to fluid flow, energetically favorable cell geometries, and alterations in mechanical response when cytoskeletal or nuclear envelope component properties are altered as in the cases of laminopathy and of vascular aging. It could also give insight into the cell polarization question by revealing whether upstream or downstream polarity is energetically favorable or has an effect on the degree or distribution of shear forces conveyed to the cell nucleus.

1.4 Objectives

The goal of this project was to develop a more realistic mechanical model of the arterial endothelial cell under flow shear stress. In order to evaluate the success of model development toward this goal, objectives were proposed as shown in the table below.

Table 1.2. Research Objectives.

Objective 1 (in silico)	to develop a more realistic mechanical model of the arterial endothelial cell under flow shear stress that can be used to evaluate the proposals: (1) that upstream polarization minimizes simulated stress on the nucleus; and (2) that nuclear envelope stiffening predicts increased reaction stress at the nucleus in the simulated model.
Objective 2 (in vitro)	to evaluate nuclear and MTOC orientation in BAECs by: (1) developing an image analysis protocol that processes MTOC and nucleus orientation efficiently; and (2) testing the prediction that that MTOC will polarize upstream under steady moderate shear.

1.4.1 In Silico Objectives

The goal of this project is to create a working computation model of an endothelial cell under fluid shear stress, which would be used to evaluate force distribution inside the cell and at the nucleus, and to investigate the effect of nuclear stiffness associated with certain human pathologies.

The first in silico object provides a way to evaluate whether the tensegrity component of the model meaningfully contributes to its mechanical properties as would be expected in a well-configured model. The second in silico objective addresses the question of whether altered nuclear envelope mechanical properties lead to a change in force transduction. If confirmed, this would provide evidence for a mechanistic link between altered nuclear mechanics in laminopathies and dysregulated gene expression.

Cell image data were used to geometrically describe the 2-dimensional layout of an arterial endothelial cell membrane and nucleus while clues found in research publications were used to estimate a topographic profile. Algorithms were constructed to generate tensegrity structures representing the cytoskeleton. A finite element approach was taken to solve the model after applying a simulated fluid pressure field to the modeled cell surface. Some concepts and files were inherited from lab members who previously worked on related projects including Nathaniel Witt, Kirstie Queener, and Tamara Al-Muhtaseb.

The target average shear stress of $15\frac{dynes}{cm^2}$ (1.5 Pa) was expected to produce smaller stresses on the nucleus due to force distribution across other cell components. It would be reasonable to expect that any force difference on the nucleus caused by moving the MTOC from upstream to downstream should be of the same order of magnitude or lower. Maximum stress differences on the order of mPa to Pa between the two MTOC polarizations might therefore be taken as confirmation of role of MTOC position in minimizing stress on nucleus. Failure of this prediction would mean that no significant difference was seen in stress distribution or maximum stress on the nucleus after MTOC relocation. This would likely indicate the tensegrity components of the model produced no significant effect in mediating force transduction from the membrane to the nucleus under moderate hemodynamic shear. The simulation could be run again with the tensegrity elements suppressed to observe whether the tensegrity structure contributed to the overall stability of the structure. The model geometry would then need to be revised in order to achieve the intended effect. It should be noted that the success or failure of this prediction is a somewhat different question than that of model validity, i.e. whether the cell polarization modulates pressure on the nucleus in live arterial cells.

In addition, the computation model of the arterial endothelial cell under flow shear stress should include these important features that would be novel improvements from previous attempts of this model:

1. The geometry of the cell should be as realistic as possible: ideally developed based on images of real cells.
2. The model should be user-friendly, and easy to manipulate and modify.

This could be accomplished by using Python to automate generation of construction points defining the cytoskeleton and external cell shape based on user-defined controls. This would require development of algorithms to generate points and connectivity data representing microtubule and actin cell structures. In the simplest case, cell shapes could be extracted from real cell images by creating a graphical user interface that allows the user to trace out relevant cell features using mouse click callbacks for graphical input of specific points in a user-provided cell image. Development of these tools could greatly increase the ease and

speed of model development while facilitating far greater structural complexity than can be practically created using existing tools.

1.4.2 In Vitro Objectives

Because intracellular forces cannot be directly measured easily, validation of the model is not a straightforward task. Cell polarization was taken as a simple though imperfect means to compare model results to live cell behavior and is the subject of the second in vitro project objective, which tests the prediction that MTOC will orient upstream of the nucleus under arterial shear stress. To achieve this goal, an automated image analysis algorithm should be developed to screen fluorescent images of MTOC and nucleus effectively.

This objective could be achieved by conducting parallel-plate flow chamber experiments to expose cells to steady shear for periods of several hours. Immunofluorescence staining could be used to visualize cytoskeletal structures and cell nuclei to observe the angle of upstream or downstream cell polarization. Control slides not subjected to shear could be simultaneously fixed and stained to provide experimental reference data. Bovine arterial endothelial cells cultured under standard conditions would be suitable material for this experiment. Use of cell lines expressing wild type lamin and cell lines expressing progerin would allow results comparison to observe whether progerin expression affects MTOC orientation relative to direction of shear flow.

Similar in vitro experiments have been performed to examine cell polarization in response to shear both by other research groups and by members of this lab in previous projects. Reported results from other groups have sometimes been contradictory while previous work within this lab group has not found statistically significant differences in cell polarization between experimental and control groups or between groups expressing progerin vs. groups expressing wild type lamin. It is possible that experimental groups were not large enough to attain sufficient statistical power to achieve significance in these experiments. In light of past work, however, it may be anticipated that no statistically significant difference in polarization will be observed between groups. In the case that orientation is observed to change in response to shear flow, this could provide evidence that MTOC position may be

used by endothelial cells to modulate the range of nuclear stress and could subsequently be used to corroborate in silico predictions of the effect of MTOC position on nuclear stresses.

This objective could be secondarily examined by investigated the question of cell polarization response to flow during wound healing. The experiment described above could be repeated after first scratching the slide in the longitudinal or normal direction relative to flow. If cells are observed to polarize in the direction of the wound, this would suggest that cells migrate to close gaps in the endothelial monolayer and that this trumps any role played by cell polarization in nuclear force management during wound healing. Cells far away from the wound site would be expected to polarize normally in agreement with results from simple flow chamber experiments. Indeed, this is the expected result based on previously published findings by other groups and on work performed previously performed by members of this lab. Should this experiment demonstrate contrary results, this could indicate a lack of sufficient data, insufficient cell confluence, or that cell migration plays a lesser role than nuclear force management in determining cell polarization at $15\frac{dynes}{cm^2}$ shear stress.

After imaging cells in phase contrast and fluorescent channels, evaluation of in vitro experimental results could be automated using Python and OpenCV to detect nucleus-MTOC pairs in cell images. The same scripts could observe polarization angle in identified pairs and perform statistical analysis on cell polarization and nuclear orientation relative to direction of shear flow. This would require careful design of algorithms to balance need for accuracy with retention of sufficient data. Development of such a tool would facilitate rapid, facile experimental results analysis while eliminating variation in results interpretation attributable to human bias, training, or experience. Careful calibration would be needed, however, to ensure accurate results.

2. METHODS

2.1 Computational Methods

The construction of a finite element model of the arterial endothelial cell was guided by a number of goals and shaped by certain inherent challenges. As pointed out in the background of this thesis, many computational models have already been developed by various research groups. This attempt, however, is distinguished by its approach, construction, and intended application. The motivation for this work, therefore, was not to replicate existing models but to address the shortcomings of such models by combining key features such as tensegrity, axial bending, and solid-body components while introducing a greater degree of geometric realism. Tensegrity models of the cell have long provided a simple and adequate tool for exploring surface response to external mechanical stimulus. In order to understand how external forces contribute to regulation of gene expression, however, it is necessary to produce a model that captures the internal transduction of forces from the cell exterior to the nucleus. This model was therefore constructed with nuclear membrane stress response as the primary target of interest. This work was intended to take an initial step toward this goal by providing a working model for future refinement.

Several key goals guided construction of the cell model. Geometric realism guided the selection of an irregular cell outline based on phase contrast images and a vertical profile dominated by a proportionally accurate protruding nucleus representing a departure from previous models which have used regular geometric shapes with a small nucleus embedded well within the interior of the cell. Fluid-mechanical simulation coupling was used rather than direct uniform loads in order to simulate real flow chamber conditions. While acknowledging that in silico models cannot capture the complexity of the cytoskeletal structure, design choices regarding tensegrity and beam element properties were guided by cytoskeletal physiology. Choice of materials and dimensions were also chosen to reflect actual material properties of the endothelial cell as far as possible considering availability of data and computational limitations.

Certain key challenges also strongly influenced model design. Flow chamber dimensions, fluid pressure and velocity definitions, and mesh shape had to be carefully tuned to achieve

acceptable fluid flow simulation results. Similarly on the mechanical side of the model, computational limits restrict the degree of complexity that can be incorporated into the cytoskeletal structure. Solution convergence is notoriously difficult when using soft-bodied materials, irregularly shaped goemetries, thin-walled membranes, and very small structures. Many simulation settings and some geometric decisions were therefore reached through a tedious process of trial and error driven by the goal of solution convergence rather than by any theoretical considerations.

2.1.1 Model Specifications

Geometry

Components of cell geometry included a plasma membrane membrane (shell), Nucleus (shell), cytoplasm (solid), Microtubules (line body), actin network (line body), and actin filaments connecting the actin network to the nucleus (line body) as shown in Figure 2.1. A rectangular prism with the dome profile of the cell cut out of the base was used to represent a flow chamber for fluid simulation **??**. In the most recent model iteration, cell height was $4\mu m$ with an ellipsoid nucleus of $9\mu m$ length, $6.867\mu m$ width, and $3.15\mu m$ height centered at $2\mu m$ above the cell base. The flow chamber was $250\mu m$ in length, $200\mu m$ in width, and $160\mu m$ in height with flow oriented along the x-axis (longitudinal) in the positive direction. It should be noted that simulated flow chamber height matched the measured height of the physical flow chamber used for in vitro experimentation. Line bodies in the actin network and nuclear actin filaments were assigned a solid circular cross-section of $7\mu m$ radius with resultimg moments of inertia $I_{xx} = 1.8583\text{e}{-9} mm^4$, $Ixy = 0 mm^4$, $I_{yy} = 1.8583\text{e}{-9} mm^4$. Microtubules were assigned a hollow circular cross-section of $30\mu m$ outer radius adn $15\mu m$ inner radius with resultimg moments of inertia $I_{xx} = 5.8834\text{e}{-7}$, $I_{xy} = 0 mm^4$, $I_{yy} = 5.8834\text{e}{-7}$. It should be noted that the large cross-sectional dimensions of the microtubules relative to the cell dimensions were due to limits in DesignModeler.

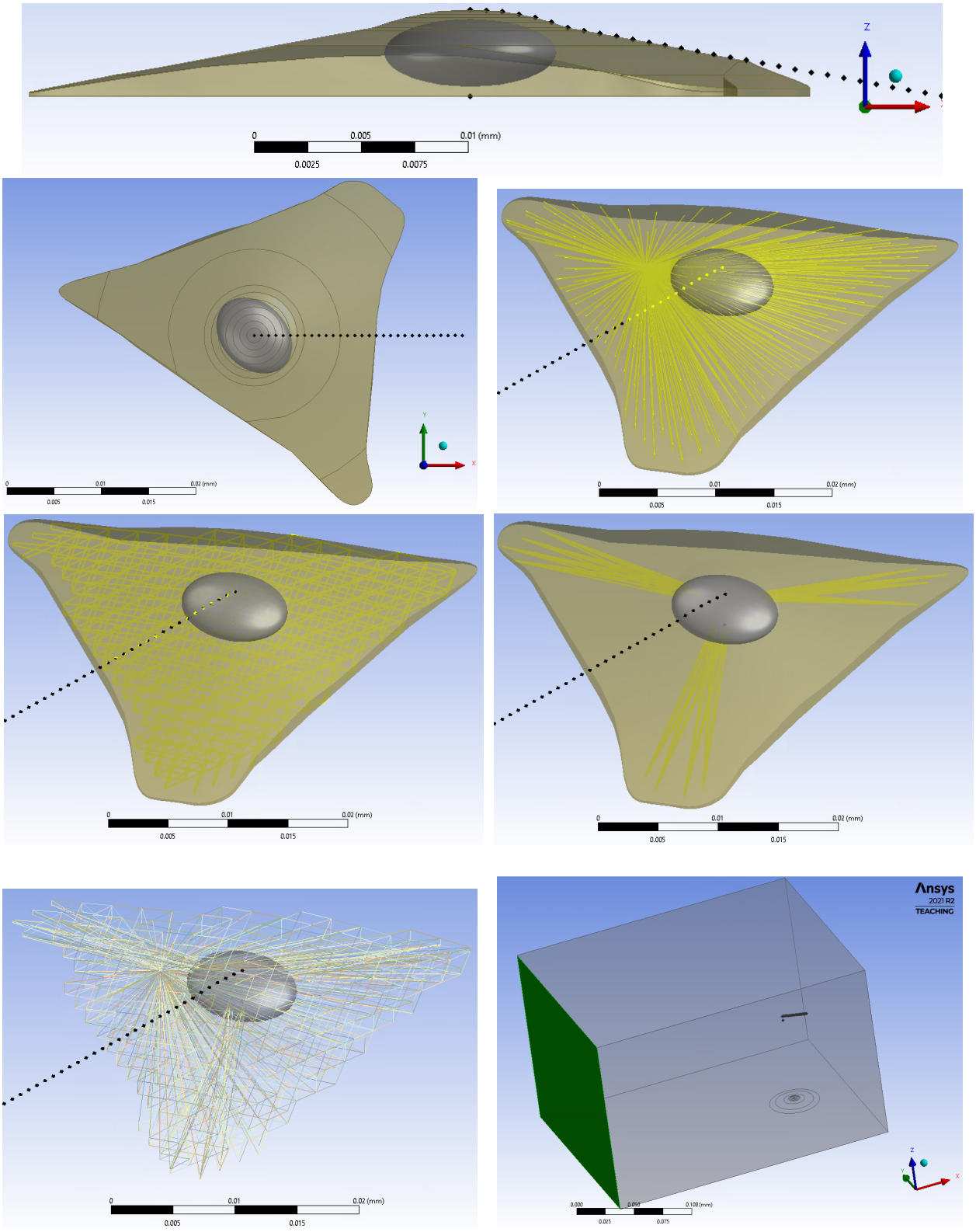

Figure 2.1. Cell Simulation Geometry Components.
From top to bottom: vertical profile, cell base profile, microtubules, actin network, nuclear actin filaments, complete cytoskeleton, flow chamber

Materials

Linear elastic materials were used for all model components due to the impracticality of obtaining accurate stress-strain curves for intracellular components. Assigned properties are shown in Table 2.1.

Table 2.1. Materials for Model Components.

Component	E	ν	k	γ	Reference
Plasma Membrane	5.45 MPa	0.45	18.17 MPa	1.8 MPa	
Nuclear Envelope	2.5 kPa	0.5	2.1 GPa	0.83 kPa	Chua [27]
Cytoplasm	250 Pa	0.5	2.1 GPa	83 Pa	Chua [27]
Microtubules	7 GPa	0.3	5.8 GPa	2.7 GPa	
Actin Filaments	1.74 GPa	0.3	1.45 GPa	0.67 GPa	Chua [27]
Nucleoplasm	5 kPa	0.5	∞	833 Pa	Jakka-Bursa [30]

E = elastic modulus, ν = Poisson's ratio, k =bulk modulus,γ = shear modulus

Fluid Simulation Settings

The steady state density-based solver in Fluent was used for fluid simulation. A laminar model was used with a fluid density of $1009kg/m^3$ and viscosity of $0.00093\frac{kg}{m\dot{s}}$ to represent cell media [33]. The inlet boundary condition was defined with a velocity magnitude of $383064(6.4\text{e}{-9} - z^2)\frac{m}{s}$ normal to the inlet face and an initial gauge pressure of 0.8Pa. The outlet boundary condition was defined by a a gauge pressure of 0Pa. All other boundaries were defined with a non-slip condition. Standard initialization relative to the inlet zone specified an initial gauge pressure of 0.14Pa and a velocity of $0.001634485\frac{m}{s}$ in the positive x direction. Implicit formulation was used for the solution with a Courant number control set to a value of 0.8.

Mesh

For the fluid simulation, the flow chamber was meshed using the multizone method with linear elements and an adaptive mesh with resolution level 6. Mesh checking was performed using the orthogonal quality criterion. Edge size controls were set to 250, 160, and 200 divisions parallel to the x, y, and z directions respectively and an edge element size of $1\mu m$ was set along the edges defining the cell cavity.

The mechanical simulation mesh used linear elements with a maximum size of $0.75\mu m$ and a skewness mesh checking criterion. A multizone mesh method was applied to the plasma membrane while triangles were used on the nucleus and an automatic method was applied to the cytoplasm. Inflation layers were used on the cytoplasm and all layers of the plasma membrane. Maximum element sizes of $0.2\mu m$, $0.5\mu m$, and $0.38\mu m$ were set for the nuclear envelope, plasma membrane, and cytoplasm body respectively. Frictionless contacts were defined between all paired faces of the cytoplasm and plasma membrane and between the cytoplasm and nuclear envelope. Node merges were applied to all vertices of line body elements to join them to the plasma membrane, to the nuclear envelope, and to other cytoskeletal parts as applicable. The nucleus interior was filled with hydrostatic fluid elements (HSFLD242) using an APDL command snippet under solver settings in the project tree.

2.1.2 Workflow

Workflow for construction of the computational model herein presented begins with generation of geometric coordinates using Python. These coordinates are used to construct a geometry in ANSYS Workbench using DesignModeler. Fluid simulation is performed in ANSYS Fluent to determine a steady state load profile which is mapped onto the upper surface of the cell model in ANSYS Mechanical. Finally, the steady state solution is simulated using the static structural module of ANSYS Mechanical within Workbench.

Geometry Generation with Python

A Python project was developed to support various tasks such as geometry generation and image analysis. Geometry scripts include a script for defining the cell profiles in the xy- and zx- planes (PyCell), a script for generating the cytoskeletal structures (PyGrid), and toolkit scripts containing assisting functions. Python packages for OpenCV, PyQt, and Numpy must be installed in the working environment in order to run these scripts.

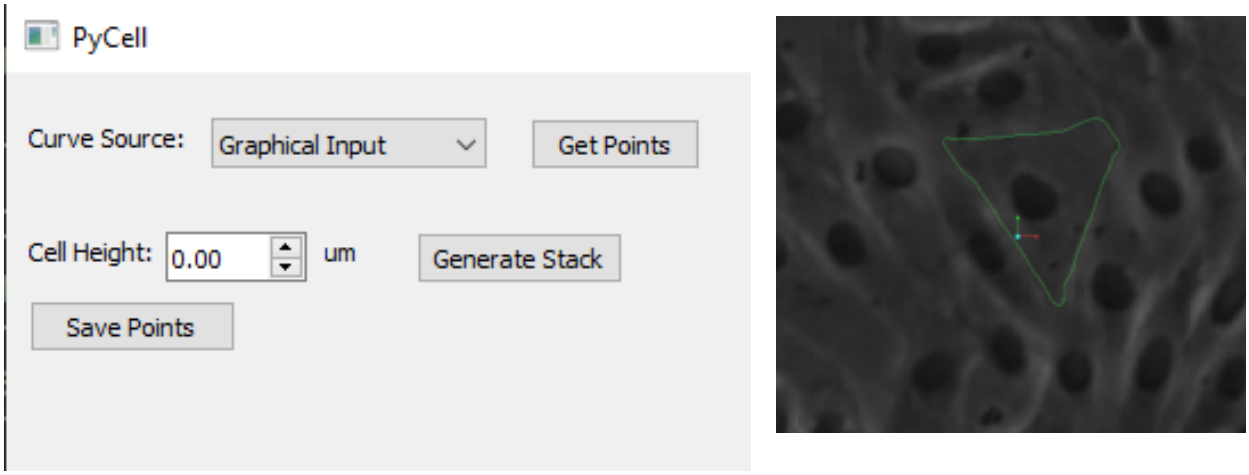

Figure 2.2. Tool for graphical selection of cell base profile.

The geometry generation process begins with the definition of the cell base shape In the xy- plane. Launching the PyCell script brings up a graphical user interface that allows the user to define a cell shape from a microscope image stored on the computer. Upon launching the selected image, the user defines the cell base by clicking points on the image to trace out the cell outline. The user then selects two points representing the major axis of the nucleus followed by two points representing the minor access of the nucleus to define the nuclear dimensions. The approximate location of the MTOC is specified by a final mouse click on the image. This information, including the center point and major axis rotation of the nucleus, is saved as a Numpy archive file. The last saved file is then automatically loaded in future launches so that the user does not have to redefine the geometry for the same cell in future work. The desired profile of the cell in the zx- plane is defined within the Python script and can be edited from that location or toggled between two currently

defined profiles. The script can also be edited to output profile points as text files in either DesignModeler or SpaceClaim readable format.

After defining the cell shape using PyCell, the cytoskeleton is generated using PyGrid. Various parameters such as cytoskeletal grid density and output file names are defined in global variables at the top of the script. After adjusting these parameters as desired, the script is run in a command terminal to generate text files defining each cytoskeletal line body as a pair of points. Each component, i.e. microtubules, actin network, and actin tethers, is saved as a separate points file.

ANSYS Workbench

After points files have been generated using Python, the simulation is completed using ANSYS Workbench. The ANSYS Workbench 2021R2 workflow for steady state analysis included three modules: Geometry, Fluent, and Static Structural. Of these modules, the Static Structural internal workflow requires the most explanation. The primary component of this module is ANSYS Mechanical with supporting input from engineering data and geometric modeling. Based on the classical ANSYS APDL workflow, the general structure of Mechanical first defines geometry, then material assignments, cross-sections, contacts, mesh, named selections, and solver settings in that order. It may be useful to discuss the key settings in each part of the workflow.

Geometry

Geometry is first defined as a stand-alone component in Workbench. Points are imported into DesignModeler as 3D curves by specifying the coordinates file for each components. Individual imports are used for the cell base, vertical profile, microtubules, actin network, and nuclear actin filaments. This allows each set of line bodies to be easily grouped together into a single part between imports which causes each component to share connections between line bodies to behave as a single entity. It should be noted that the actin network must be imported as two files in cases where more than 1000 individual segments are present due to maximum limits in DesignModeler. The upper and lower actin network regions should also

be connected along the cell perimeter by manual line body definitions to make the structure more stable. Additionally, the dome profile must be imported as individual construction points rather than as a 3D curve. These points are then connected by manual selection. This avoids the problem of geometric gaps which unavoidably develop between the cytoplasm and plasma membrane due to the impreciseness of smooth curve interpolation used in a 3D curve import 2.3. Such gaps become more severe as the scale of the model decreases and are therefore problematic for micron-scale geometries. This is not an issue for cytoskeletal elements since each imported segment contains only two points.

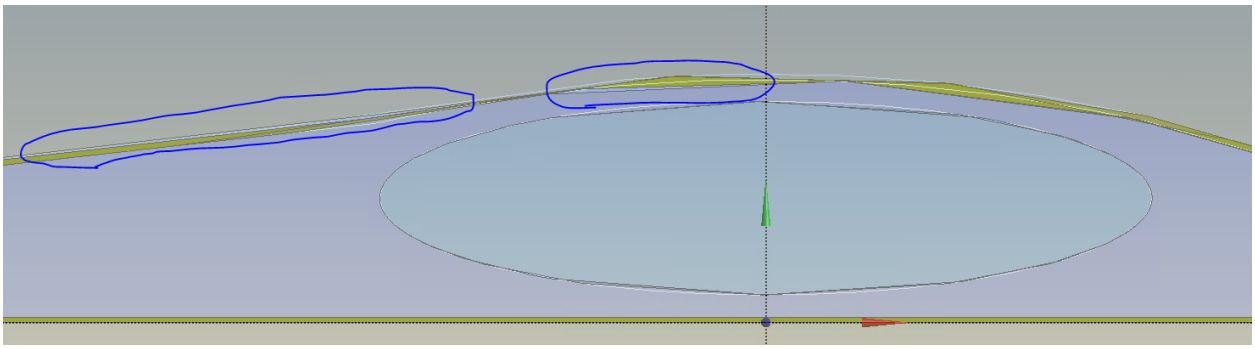

Figure 2.3. 3D Curve import method results in geometric gaps.

The cell geometry is generated from these curves by first rotating the dome profile about the z-axis and retaining the intersection of this dome with an extrusion of the cell base to form the cytoplasm. Surfaces created from the resulting faces form the plasma membrane. The nucleus is created as a scaled thin-walled sphere while the flow chamber is formed by subtracting the full cell dome from a rectangular prism. Cross-sections and named selections may also be defined for use in Fluent or Mechanical.

Fluent

After transferring the model geometry from the geometry component to the Fluent module, the transfer link is removed to allow edits. All geometric components except the flow chamber are then suppressed in DesignModeler before opening Fluent Meshing. Named selections are then applied to appropriate faces including "inlet," "outlet," "wall," and "wall-deform." These names are recognized in Fluent to identify regions for boundary conditions.

Mesh settings may be adjusted before generating the mesh. It should be noted that a high degree of orthogonality is required to obtain accurate results and that the mesh should therefore be generated using a hex-dominant or multizone method. After meshing, solution parameters and controls are adjusted in Fluent before calculating a solution. Special attention should be paid to the solver type and initialization conditions. Finally, the solution results should be checked in CFD-Post to ensure that velocities, pressure profiles, and shear stress profiles behave as expected.

Mechanical: Geometry

The geometry section of Mechanical imports the geometric components defined in either DesignModeler or SpaceClaim and allows material assignment for each part from those materials previously defined in the Engineering Data section of the module. Thicknesses must be entered for shell bodies. For uniaxial elements, a cross-section and element type must be assigned to each part. Cross-sections determine the moment of inertia equations for use in populating the stiffness matrix while the element type determines the behavior and degrees of freedom. Available choices include truss elements (LINK180), beams (BEAM188), or cables (CABLE280). Unlike links, beams allow bending to take place within the element and were used in most model iterations to describe microtubules following the example set in the bendo-tensegrity model discussed previously [30]. Cables react only under tension forces and were used in advanced model iterations to represent actin fibers including the cell cortex and the nuclear tethers. Furthermore, the geometry section allows specific APDL command snippets to be applied to each geometric part. This could be useful for assigning material properties directly, altering the direction of surface normals, etc. In practice, however, this feature was generally not used in model development. Virtual topology is also a useful feature for causing connecting faces within a body to behave as one and may be added to the geometry section by right-clicking on the Model folder in the project tree.

Mechanical: Connections

Connections in ANSYS Mechanical define the mathematical rules governing the physical boundaries between each geometric part. Without defined connections, solid parts may be free to pass through each other without interaction and will fail to transfer loads between bodies. Connections are defined only for solid parts and not for the boundaries between solid bodies and regions of hydrostatic fluid elements. Either closed or open contacts are allowed depending on the contact type. A closed connection is one in which the parts are expected to be in direct contact while open connections need not be in initial contact. The latter is useful for situations in which one body is initially separated from another body but could come in direct contact once the cell has deformed under load. By default, all connections are automatically generated. This frequently causes unwanted behavior, particularly when redundancies are created after geometry updates, and may lead to convergence issues. Automatic connections should be turned off from the main Workbench window. Important connections in this model include the plasma membrane to the cytoplasm and the cytoplasm to the nucleus. In versions of the model which attempted to use hydrostatic elements for the cytoplasm, the key connections were between the plasma membrane and the nucleus and between the plasma membrane upper face and the plasma membrane lower face.

Several connection types are made available in ANSYS Mechanical, but the two which were found to be useful for this model were Bonded and Frictionless contacts. Bonded contacts are modeled as though the intersecting faces are glued at the boundary. Contacting nodes remain in contact for normal and tangential forces of any magnitude. This is the default contact type and is appropriate for surfaces which should remain in direct contact throughout the simulation, making it applicable only to closed contact geometries. Frictionless contacts, on the other hand, allow paired surfaces to move freely relative to each other while preventing penetration. Normal forces may go to infinity only in penetration and are zero otherwise while tangential force transfer is always zero. This can be appropriate for open contact geometries to prevent penetration following model deformation or for initially closed geometries which are not bound to each other. In either contact type, one surface is described as the contact surface and the other as the target surface. As a general

rule, the flatter or more stationary object should be designated as the target. An option is also available to specify whether the top or bottom of the surface is to be used for contact detection.

Various settings may be adjusted for each contact. These are program controlled by default, but adjustment may be necessary in some cases to achieve appropriate model behavior. For both contact types used in the cell models, the penetration tolerance defines how far the contact body may penetrate the contact. The program must also define how close elements of either object must be to each other in order to be considered in contact. This is defined by the pinball radius setting. Geometry correction allows minor geometric adjustments to ensure that contacts behave as desired. Model iterations which contained geometry correction were set to adjust to touch in order to minimize small gaps between contacting bodies due to imperfections in the geometric rendering. Contact stabilization is also an option to prevent bodies which are not initially in contact from failing in early load steps and is controlled by a damping factor between 0 and 1. Since stabilization force does not represent any real force, this option should be used only when necessary and the damping factor should be kept as small as possible.

The contact tool may be inserted at the end of the Connections section to provide invaluable feedback on contact quality. This tool evaluates each defined contact pair to determine whether the contact is far open, closed, questionable, or problematic according to evaluation criteria. It also returns information on such details as the initial penetration depth, gap size, and pinball radius for each contact pair. Although this tool is placed before the meshing step in the model workflow, the contact tool requires a completed mesh in order to evaluate results. For an efficient work flow, the contact tool should be used to evaluate the state of all contacts under current mesh settings to reveal any problems before proceeding to solve the model.

Mechanical: Meshing

Perhaps the most important factor in achieving convergence of a solution for the model is constructing an appropriate mesh. The cell model developed aims to be extendable to ir-

regular geometries in order to facilitate geometric realism. Sharp corners, thin solid sections, and irregular asymmetric profiles make mesh generation a challenging task. A poorly constructed mesh may either fail to generate or lead to excessive distortion and non-convergence when solving the model. Many options are available to tune mesh parameters before mesh generation and to edit the mesh afterward.

Within the top-level settings, mesh physics offers several alternatives to the standard mechanical mesher. The most interesting of these is the nonlinear mechanical mesher. Unfortunately, this option was found to be unable to complete the task of mesh generation on some bodies but could be a good alternative for simplified models. The mesh size may also be explicitly defined or an adaptive mesh may be implemented. The latter option allows choice of mesh resolution on a scale from 1 to 7 with 7 representing the finest mesh option available. A maximum element size may be specified in addition to this in order to achieve a yet finer mesh as was found to be necessary in advanced model iterations. Auto-inflation controls allow the mesher to attempt inflation on solid bodies but are not applicable to shell bodies. Default settings are generally appropriate for most other assembly-level mesh parameters.

In addition to assembly-level controls, additional mesh controls may be applied to individual bodies, faces, and edges. Inflation allows the mesh to be shaped by a physical boundary. This helps to avoid problematic mesh around sharp corners or irregular curves and is especially useful on the plasma membrane of the model and on the outer faces of the cytoplasm. Mesh method allows several useful options for the basic approach to meshing and the dominant element type. For example, quadrilateral elements may be highly appropriate for regularly shaped flat membranes but triangles tend to be less problematic for the irregular geometry of the plasma membrane and have also been found to perform better than quadrilateral elements for the highly curved ellipsoid shell representing the nuclear membrane. Face sizing, body sizing, and edge sizing may also be applied to individual features of the model and often prove helpful at resolving the unique challenges of a single face or body. Many other features such as mesh matching, refinement depth, and face mapping were experimented with but found to be of little use for the model versions developed in this project.

After the mesh is complete, mesh edits may be applied. The most useful of these is the node merge command. This allows bodies, surfaces, edges, or vertices from adjacent bodies to be joined. Two nodes that are in near proximity are replaced by a single node. For example, a node merge between a microtubule vertice and the plasma membrane face will cause the node at the end of the microtubule to also be a node in the plasma membrane providing that the original nodes are within a defined proximity. In this model, this feature is primarily used for joining cytoskeletal elements to shell elements, i.e. the plasma membrane and nuclear envelope. This is necessary because the cytoskeleton must be connected to other cell bodies in order to mediate force transduction and provide structural support to the cell. Node merge rather than contact regions should be used to accomplish this in order to avoid solution error.

Mechanical: Solver Settings

A fixed displacement boundary condition may be imposed to secure the lower face of the cell or the glass slide. The pressures derived in Fluent at the location of the cell surface were mapped onto the upper surface of the plasma membrane using the import load feature. Because the cell in the model represents one component of an endothelial monolayer, pressures are mapped onto the upper plasma membrane only and not onto lateral surfaces of the cell. It should noted that although ANSYS refers to the mapped load as a pressure, the load actually applies the vector sum of pressure and shear forces at each node. This load should be checked carefully to make sure it falls within the expected range. Additional solver controls such as time stepping options can be useful for addressing any issues with solver convergence.

2.1.3 Decision Points and Challenges

Software Selection

Choice of software tools included many factors and the outcome of decision made yielded lessons which could improve future work. At the beginning of my work on this project, groundwork had already been laid using ANSYS Workbench. In addition to this, ANSYS

was the only commercial license available within our group. This prevented serious consideration of COMSOL or Abaqus. Therefore by continuity with previous work and software availability, ANSYS appeared to be a natural choice. In addition to this, ANSYS is known to have advanced tools for non-linear analysis which seemed to be a key advantage for geometrically realistic soft-body analysis. From the start, however, many problems were encountered while using the software which made it necessary to consider alternatives to Workbench both within the ANSYS product family as well as open-source finite element packages.

FEBio was the primary alternative to ANSYS that was considered. This open-source package originally developed by MIT researchers presented several advantages. FEBio was specifically designed for biomechanics problems and comes with a library of non-linear materials representing various bodily tissues albeit without any predesigned intracellular materials. The software was also originally built to be run in headless mode with a GUI tool added later in development. Thus, at its heart, FEBio is designed to be scriptable which simplifies automation for parametric analysis of models. Generated simulation files are written as XML which further simplifies the process of building custom controls or fine tuning model specifics. Fluid-solid interaction is by design one of the key features of FEBio making it particularly attractive for our task of modeling endothelial cells under hemodynamic shear. Finally, fairly comprehensive online documentation is available. Despite these advantages, however, some drawbacks remain. The software is still only a few years old and still has much room for development before reaching its full potential. At the same time, it does not receive frequent developer updates. During limited experimentation with the software, occasional crashes were observed similar to those observed with ANSYS. Perhaps the greatest drawback, however, was the absence of one-dimensional elements. This is an important feature for tensegrity structures. Although the open-source nature of the FEBio suite makes it possible to add such a feature, this could take significant time.

Other software alternatives were also considered. Many open-source software tools such as FENICS and SfePy could possibly be viable alternatives to ANSYS for future work. None appeared after limited comparison of features to be perfectly suited to the project at hand without significant custom development to add additional features such as one-dimensional truss elements. Within the ANSYS family of products, LS-Dyna and APDL

Mechanical were considered. LS-Dyna has the advantages of being highly scriptable and well-suited to non-linear analysis. Documentation, however, is frequently reputed to be incomplete and the high-impact non-linear analysis which is the key application of LS-Dyna appeared to be unnecessary for modeling cells under constant shear flow. APDL Mechanical has the particular strength of being highly scriptable, but it was found that APDL scripting could be easily incorporated into Workbench while APDL Mechanical does not appear to be well-suited for modeling of fluid-solid interaction. All things considered, these cursory investigations into Workbench alternatives did not result in the discovery of an ideal simulation tool. With sufficient time, however, further exploration might yield more interesting alternatives.

Furthermore, while such an endeavor was beyond the scope of the current study in light of current goals and time constraints, it is highly recommended for future work to develop a custom finite element analysis tool specifically for modeling endothelial cell mechanics. This prospect presents numerous potential advantages. It would allow the software to be optimized for this specific application, saving computational resources and easing burden on the end user. At the same time, it would avoid license access issues which have frequently obstructed this project. This approach would also be more easily distributable to other research groups by avoiding the necessity of obtaining a license for proprietary software. Finally, it would allow full control over simulation parameters and full transparency regarding the mathematical basis for each aspect of the finite element analysis.

2D vs. 3D Analysis

In light of the complexity of the model and the many obstacles to achieving model convergence, the possibility of a preliminary 2D analysis was considered. Several potential advantages recommended this approach. Firstly, reducing the geometric complexity of the problem might yield clues as to the expected general behavior of the system to help evaluate the accuracy of results in the more complex 3D model. Secondly, the far lower computational demands of a 2D model would allow rapid iterations of various design ideas to help inform a more efficient and appropriate 3D design. In addition, the reduced size of the model would

allow it to be run on student versions of the ANSYS license, allowing work to continue during the frequent instances of difficulty accessing the full software using shared resources. Beacuse of these apparent advantages a 2D model was attempted, but it was found that ANSYS Workbench does not support line bodies in 2D models. This limitation would have eliminated the cytoskeletal component of the model, drastically limiting the applicability of any findings to the construction of the full 3D model and making direct application to the computational predictions impossible. For this reason, plans to construct a 2D version of the model were abandoned.

Geometry Editors

ANSYS Workbench has two built-in geometry editors: DesignModeler and SpaceClaim. Additionally, both editors come with CAD import capability to allow most of the modeling to be performed externally. At the start of my work on this project, existing files made use of DesignModeler with CAD imports built in Creo Parametric in some cases. DesignModeler features flexibility with a low learning curve. Furthermore, the grouping of geometry features into DesignModeler Parts provides a convenient and simple way to ensure that these objects are treated as single entities in the mechanical editor without the need for internal contacts or node merges. Geometric operations can be scripted using javascript, but documentation for scripting appeared to be nearly non-existent. SpaceClaim appeared to have a steeper learning curve, but its Python-based geometry scripting was found to be far more accessible. A record button in SpaceClaim allows all GUI options to generate the script equivalent of each command making SpaceClaim an attractive tool for automating geometry feature generation.

External geometry editors such as Autodesk Fusion or Creo Parametric were not used to generate structures. Such software does not appear to contain options for generation of one-dimensional line bodies used for tensegrity trusses. While these could be added in after importing the files into Workbench, the need to perform additional geometry editing in Workbench diminishes any advantage of using an external editor. Furthermore, in order to prevent unwanted geometric penetration between various structures, it was thought desir-

able to specify exact intersection coordinates between cytoskeletal elements and the plasma membrane. This could be accomplished in either DesignModeler or SpaceClaim by importing a points file containing coordinates and then generating both plasma membrane geometry and cytoskeletal geometry using the same set of points. A similar task could have been accomplished using SolidPython and OpenSCAD, but this is best suited for simple geometries. From the above considerations, it was determined to use DesignModeler throughout most of this project. Automating SpaceClaim using Python remains an interesting prospect for future exploration, however. The generation of points files imported into DesignModeler is described elsewhere in this report.

Fluid Modeling

ANSYS Workbench contains two primary options for fluid modeling: Fluent and CFX. The previous work performed on this project had made use of Fluent and no significant shortcomings of the software were observed to motivate consideration of CFX as a replacement. Export controls present in CFX could prove useful in future work, but errors encountered in CFX visualization tools made the module an unattractive option for the present. In any case, fluid results should be checked for appropriate convergence, especially if very large maximum pressures are obtained from the simulation. Convergence errors were briefly encountered in the course of this project and were rectified by optimizing the mesh of the flow chamber for element orthogonality.

It was determined to simulate fluid flow through the flow chamber to obtain steady state results and then to map those results onto the upper surface of the endothelial cell for ramped loading over one second in a static structural analysis. A more accurate alternative might be to create a coupled system in which the fluid solution is re-evaluated at every time step based on the deformation observed in the cell and this new fluid solution is used to solve the cell structural analysis for the next time step. While this approach may be expected to produce more accurate results, it would be much more computationally expensive and is therefore ill-suited to initial troubleshooting of the model. It would be interesting to explore in future

work whether such additional computational cost is warranted by the ultimate difference in final result.

Python Scripting

Much of the cell geometry generation was automated using Python to facilitate parametric simulations and rapid geometry updates. For this purpose, the xy-plane was chosen to represent the glass slide to which the cell is affixed during flow experiments with the z-axis providing volumetric depth to the model. A major goal of this model is to improve upon past work by other groups to expand model applicability to realistic geometrically irregular shapes. An obvious method to accomplish this goal was to allow the user to acquire arbitrary cell shapes from real images of endothelial cells. This was accomplished by building a simple GUI using PyQt5 and OpenCV which would allow the user to select an image of the desired cell. Initial attempts at automatic edge detection using the Canny algorithm which is a built-in feature of OpenCV proved to be problematic due to low contrast at cell boundaries of test images. While this problem could be revisited in the future, a simple present solution was to have the user click points on the image to trace out the cell outline and select important features. In the future, this program could easily be expanded to allow the user to select certain realistic predefined shapes whose dimensions are dependent upon parameter input provided by the user.

Cell Geometry Decision Points

Orthogonal Profile

The images available to provide a template for the cell base outline did not provide information regarding the cell profile in any orthogonal plane. While such information could theoretically be constructed using fluorescence microscopy, such data was not readily available. It was therefore necessary to make a reasonable estimate of the cell profile in the xz-plane. In contrariety to existing endothelial cell models which tend to place the nucleus as an embedded structure within some type of convex dome, the Hazel and Pedley model described earlier in this thesis represented the endothelial cell profile as that of a raised

nucleus [17]. This profile description of a membrane stretched over a raised nucleus appears to agree with both conventional diagrams of endothelial cells and atomic force microscopy studies as shown in Figures 1.7, 2.4. It was initially decided to model the endothelial cell profile as a Gaussian curve. This approach has the advantage of being geometrically simple and mathematically well-defined while approximating the profile of a live endothelial cell. The Gaussian shape, however, leads to some cytoskeletal elements protruding through the plasma membrane in the constructed model near the curve inflection region. This problem was solved by modeling the cell profile as a cone with a rounded cap. This was implemented using a piecewise defined function with a central arc to form the cap of the dome and straight linear sections to form the slanted sides of the dome. One possible disadvantage to either approach is the radial symmetry displayed by a 3D dome which does wholly agree with AFM studies. The effect of this difference could be investigated in future work, however, by scaling the dome anisotropically with respect to the orientation of the nucleus.

The height of the cell was approximated by comparing values from various sources. The sources described above for suggesting the cell profile shape also suggest a range of values for cell heights ranging from 2 to 6 m. A median value of 4 m was selected for the plasma membrane height such that the cell nucleus would not protrude through the cell membrane. In order to form the 3D cell geometry, a Gaussian curve following the equation $z = h^2 \mathrm{e}^{\frac{-x^2}{2s^2}}$, where h represents the cell height and s represents the horizontal spread, was rotated about the z-axis to form a dome. The cell base outline was drawn as a closed loop spline curve using the point acquired as previously described. The intersection of the Gaussian dome with an irregular prism extruded from the cell base was then taken as the volume of the cell. Thin surfaces created from the faces of the resulting solid formed the plasma membrane of the cell. By enclosing a prominent nucleus in a concave membrane,

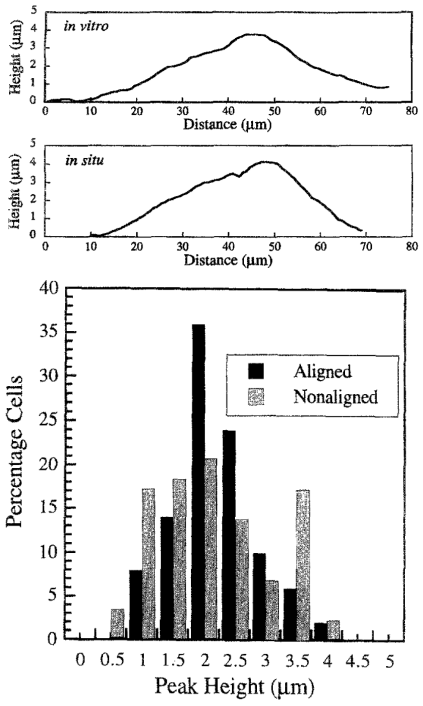

Figure 2.4. RAEC topology. Atomic force microscopy of rabbit arterial endothelial cell profile [34]

this geometry represents an improvement over existing published models in the area of geometric realism. As discussed further elsewhere in this thesis, this realism brings with it greater difficulty in achieving convergence of the simulation due in part to the presence of thin structures with irregular edges.

Geometric Construction Method

The construction method of the cell volume represents an important decision point. In particular, the decision to use vertical spline curves, horizontal spline curves, a single rotated spline curve, or a single rotate polyline had significant implications for model geometry. In the first model iteration, four vertical spline curves orthogonal to the cell base were constructed to create a skeleton for the cell. A skin was then swept over these spline curves. This approach, though reasonable for a convex dome, was not well-suited for creating the desired profile with a prominent raised nucleus.

In order to explore horizontal spline curves, an algorithm was developed to produce defining points for each layer using Python. This approach envisioned the cell surface like a topographic map. Starting from the cell base profile, each layer would take a step upward along the z-axis to define a parallel plane. For each layer, the script iterated through each point in the previous layer. Within the plane, each new point was defined by starting from the corresponding point in the previous layer and taking one step inward. The direction of this step was defined by drawing a line between the two points on either side of the current point in the curve and stepping normal to that line. A built-in OpenCV function was used to ensure that the direction was correct by checking whether the new point was contained within the polygonal curve described by the previous layer. The magnitude of the step was determined by normalizing the step size based upon the planar distance of the point to the center of the cell nucleus relative to the number of layer steps remaining to be drawn. This algorithm was found to produce self-intersecting lines at sharp corners in some cases. Therefore, the algorithm was modified to check each curve for self-intersection and to iteratively drop out a point near the intersection until no further self-intersection was detected. In this way, the number of points grew lesser as the layer height increased. When plotted afterwards,

the result of this algorithm showed smoothly increasing topological layers to define the cell topology with no sharp edges. The drawback to this approach was not made clear until the curves were imported into DesignModeler. The interpolation used for the closed spline curves for each layer appeared to be variously interpreted giving the cell a knobby appearance with many protrusions and overhanging layers. This effect was not improved by increasing the number of layers. The model was also highly sensitive to the starting location of each curve, failing to successfully import in most cases. Unfortunately, no means was discovered to either view nor modify the spline fitting formula used by DesignModeler making this approach ultimately untenable.

The third method of defining a single Gaussian curve in the xz-plane and rotating it about the z-axis to produce a topology was found to be both simpler and more successful. It did not produce the adaptive step featured in the layered approach and also produced sharp edges where the dome intersected with the cell base extrusion. This approach also led to very thin structures near the edges of the cell, creating some challenges both for meshing and for avoiding protrusion of cytoskeletal elements through the cell membrane and caused gaps to form between the plasma membrane and cytoplasm. These drawbacks were ultimately overcome by using a rounded cone structure defined by a polyline rather than a Gaussian structure defined by a spline curve.

Cytoplasm

The cytoplasm of the cell could be approached in several ways. The cytoplasm could be left out of the model as is the case in existing pure tensegrity models of the cell, modeled as a solid with a low elastic modulus, or modeled as a hydrostatic fluid. The initial model at the beginning of this project took the approach of modeling the cytoplasm as a weak solid. Due to its low elastic modulus, however, this approach led to great difficulty in achieving convergence due to high elastic deformation and problematic contact geometry while contributing very little to the mechanical structure of the cell. Defining a high bulk modulus improved the expected mechanical contribution by decreasing compressibility but did not at first resolve the repeated issues with convergence. Indeed, a test model applying

very low constant pressure loads to the cell found the cytoplasm, either liquid or solid, as the primary obstacle in achieving solution convergence.

Initial success was encountered using hydrostatic fluid elements (HSFLD242) to model the cytoplasm. This type of element uses a single common center node for all elements and forms the elements by connecting that center point to all nodes on a given enclosed surface. This allows loads to be transferred across the entire enclosing surface. The command to create such elements is not available as a GUI button in Workbench 2021 but may be formed by leaving the fluid region void during initial meshing and inserting an APDL command snippet under the solution settings. Hydrostatic element formation is sensitive to the normal direction of the surface. It is therefore necessary to observe solver output for reports of negative fluid elements and to flip the membrane surface normal direction in DesignModeler if necessary. Alternatively, it is possible to reverse the surface numbering order in the APDL command snippet using the TLAB, reverse command. Furthermore, it is possible to make the fluid compressible or incompressible and to assign an elastic modulus for viscoelastic effect. In order to learn about this element type, a simple fluid-filled sphere model was built. The sphere shell was assigned a hyperelastic material and fixed to a pedestal. Another smaller sphere was embedded within the structure to represent a nucleus. Applying a point load to the outer sphere, a reasonable solution was readily obtained. Several lessons were learned from this experiment. Firstly, the number and placement of hydrostatic center nodes did not affect the results. In other words, the results were the same for a single set of hydrostatic elements sharing a node at the center of the sphere or for multiple sets of hydrostatic elements with nodes variously placed between the inner and outer spheres. Secondly, it was possible to make the nucleus either fluid or solid, but in neither case was hydrostatic pressure observed to be transferred to the surface of the embedded nucleus. This remained true in cases where both the inner sphere and the outer sphere were chosen as surfaces for the same set of hydrostatic elements. Thirdly, it was necessary to tether the inner sphere using beam or cable elements to prevent it from floating away from the structure during the solving process. In addition to this simplified learning model, convergence was achieved with mostly reasonable results in a more complex model using an arbitrary spline curve as the cell base and a shallow convex dome as the upper cell surface. In this case also, however, hydrostatic

pressures inexplicably did not result in stress on the cell nucleus. Despite the convergence achieved in both of these test models, however, hydrostatic elements were not found to produce a convergent solution in the geometrically realistic model of the endothelial cell nor was any center node placement found which could entirely avoid the problem of negative hydrostatic elements. This remained true despite extensive troubleshooting varying the central node placement, all possible combinations of surface normal directions, and surface region selections. This issue ultimately led to the decision to revert to a solid model of the cytoplasm. After much experimentation, a combination of mesh settings was discovered which facilitated solution convergence of the cytoplasm modeled as a weak solid.

Nucleus

Decisions for nuclear geometry included dimensions, material selection, and geometric methods. Construction of a three-dimensional ellipsoid is not a mathematically trivial task. It was therefore determined to draw the nucleus as a sphere using the dimension of the desired major axis before scaling the sphere anisotropically to achieve the desired minor axes of the ellipsoid. Nuclear dimensions and major axis rotation were determined from the user selection of major and minor axis obtained at the same time as the cell base profile as previously described. As with the cytoplasm, the case could be made for either a solid or hydrostatic fluid to form the volume of the nucleus. The solid modeling approach is the geometrically simpler option and has been used in previously published models. In such models, it is represented by a material of very low elastic modulus. This renders the nucleus subject to extreme distortion and raises the question of whether it accurately models the structural contribution of the nucleus which may be due largely to its incompressibility. Assignment of a high bulk modulus may be one solution to improving the nuclear mechanical properties in a solid model.

In a real cell, the nucleus consists of both an inner and an outer nuclear membrane separated by a small gap (50 nm) but connected by nuclear pores and LINC proteins. The interior of the nucleus is filled with nucleoplasm high in chromatin content resulting in a viscoelastic fluid. This arrangement could perhaps be best modeled using a double

membrane filled with viscoelastic hydrostatic fluid. This approach was attempted in the model. Indeed, the double membrane is necessitated in such an approach because the surface normals of the nuclear membrane must be oriented in opposite directions when implementing the fluid enclosed by the nucleus and that enclosed by the cytoplasm. LINC proteins were also included in some versions of the model after being generated using Python as described below. Once solver convergence issues caused be the cytoplasm were overcome, it was found that good results could be obtained by modeling the nucleus as a thin single-layer membrane enclosing a viscoelastic hydrostatic fluid.

Cytoskeleton

The cytoskeletal components were generated using Python and include microtubules, actin bundles, actin cortex, and optional connecting structures including integrins and LINCs. The actin cortex was created as a network of actin fibers lining the inside surfaces of the plasma membrane and joining the microtubule ends with tensile elements. Actin tethers were used to secure the nucleus within the cell. The inclusion of these elements was based on aforementioned experiments with the simplified fluid sac model and served as a highly simplified representation of the connections between the actin network and the nuclear membrane in live cells. Integrins and LINCs were optionally modeled using the same element type used for actin filaments and were embedded in the plasma membrane or nucleus respectively. These were oriented normal to the surface and assigned a length of 150 nm for integrins or 300 nm for LINCs in order to ensure that they extended through the membrane. Both integrins and LINCs were made as optional experimental features which were included in some versions of the model. Practical motivations for including integrins and LINCs respectively were to offset cytoskeletal elements from the plasma membrane to reduce penetration and to provide a line body connection between the inner and outer nuclear membrane. These motivations were made obsolete by the decisions to move away from a Gaussian profile for the plasma membrane and to use a single membrane to represent the nuclear envelope. Therefore, integrins and LINCs were not included in the latest versions of the model.

For the automated generation of cytoskeletal structures, it was necessary to create common nodes in close proximity to the plasma membrane which could be shared by multiple cytoskeletal elements. Two different algorithms were considered for accomplishing this goal. A random growth model was first considered which would have created each new node by starting from one end of the cell and picking each new node based on a random angle and step size, discarding any nodes which fell outside the cell volume. Such an approach was envisioned to recreate the complexity of the cellular cytoskeleton on a smaller scale. The second method considered was to overlay the cell with a rectangular grid and to discard all grid points which fell outside the area of the cell base profile. This second method was chosen over the first due to its advantages in reproducibility, simple user control based on grid density, and ease of implementation.

Once the common nodes of the grid had been identified, the base layer of the actin cortex was formed by iterating over each row of the grid. For each point, three links were created including the next point in the same row, that in the previous row, and that in the next row. In this way, every interior point of the grid was connected to four other points, creating a fine meshwork. In order to generate the upper actin cortex, the same process was used with a copy of the grid which was projected onto the upper surface of the plasma membrane by using calculating the z-coordinate of the point based on its planar radial distance from the center of the cell nucleus. This entire process was repeated in miniature to create a smaller, denser grid on the upper surface of the cell nucleus.

Once the grid nodes for both the upper and lower surfaces of the actin cortex had been assigned, microtubules were created very simply by linking each point in either grid to a single node representing the MTOC. Actin tethers required a special approach to avoid protrusion through the concave part of the plasma membrane. The goal of these structures, as stated before, was to anchor the nucleus in the cell using tensile load-bearing elements. In order to accomplish this, the cell was conceptually divided into radial zones equal to the number of corners in the cell. In the case of the roughly triangular cell shape described in this work, three zones were present. Each zone was defined angularly by drawing a line from the center of the nucleus to the respective corner of the cell and then taking the bounds as $\pm\theta$ from that line. A cell attachment arc region was defined by specifying a minimum and maximum

distance from the cell center which were chosen such as to prevent protrusion of the resulting fiber through the plasma membrane. The attachment zone was then searched from the outer arc toward the center until a specified number of grid points had been located within the attachment zone. This same process was repeated to find the nuclear attachment site on the upper surface of the cell nucleus. Once all attachment points had been identified, they were connected by drawing three connecting tethers from each plasma membrane attachment site to nuclear attachment sites in the corresponding zone. Each value described could be easily parameterized by the user. For the purposes of this study, the cell was defined with three zones of $\pm 15^o$ degrees with four pairs of attachment points in each zone, resulting in the generation of 12 actin tethers in each of the three zones. Once all these structures had been created, they were exported as sets of point coordinates in text files and formatted for import into DesignModeler. Once imported into DesignModeler, each set of lines was grouped to create its corresponding part; namely, microtubules, actin cortex, actin tethers, integrins, or LINCs.

2.2 In Vitro Methods

2.2.1 Cell Culture

Bovine arterial endothelial cells between passages 6-12 were cultured at 37 degrees Celsius at 5% CO2. Dulbeccos modified Eagle medium (DMEM) was fortified with 1% L-glutamine, 10% fetal bovine serum, and 2% Penicillin-Streptomycin. Cells in T75 flasks were fed with 10 mL cell media every 2-3 days. Upon reaching confluence, cells were passaged at 1:3 in most cases to maintain cell lines or as needed to prepare experimental slides. During the flow experiment phase of research, cells between passage 8 and 12 were plated from T75 flasks onto glass slides. At each plating, cells were divided as required. In most cases, half of cell by volume were passaged into new flasks to maintain the cell line while a quarter of cells were plated onto each of two microscope slides, one to be used as an experimental slide and one to be used as a control. Plated cells were placed in petri dishes and cultured until suitable progress toward confluence was reached.

2.2.2 Flow Experiments

After attaining between 50-100% confluence, plated cells were placed in a flow chamber containing a slit at either end to serve as the inlet and outlet. A flow apparatus similar to that described by Frangos et al. [6] was intended to produce a constant shear of approximately 15 dynes/cm over the cells. Flow cabinets maintained environmental controls for carbon dioxide and temperature (37 °C) The flow chamber was machined from clear polycarbonate using a CNC router by lab machinist Kevin Carr. Interior dimensions were 38 mm in width with 72 mm between the inlet and outlet slits. The four flow chambers used in this experiment averaged 1086±20 μm in interior height leaving an approximate average 160 μm flow height after accounting for the microscope slide of approximate 930 μm thickness. The column height of the flow apparatus was 35 cm between inlet and outlet to produce a constant pressure of 3.46 kPa as calculated in the equation

$$P = \rho g h$$

where the density of the cell culture medium (ρ) is estimated at 1009 $\frac{kg}{m^3}$ [33], g is the acceleration due to gravity and h is the column height. Cell culture medium viscosity (μ) is estimated at 0.930 $mPa \cdot s$ [33]. It can be shown from the Navier-Stokes equation that

$$Q = \frac{2b(\frac{h}{2})^2 \Delta P}{3\mu l}$$

where Q is the volumetric flow rate, b is the width of the flow chamber, l is the length between the inlet and outlet, and ΔP is the pressure drop between the inlet and outlet. Assuming that relative pressure goes to 0 Pa at the outlet, this results in an estimated volumetric flow rate of 0.6805 $\frac{cm^3}{s}$. It can also be shown from the Navier-Stokes equation that

$$\tau = \frac{6Q\mu}{bh^2}$$

where τ is shear stress at the plate. Shear stress estimates were calculated using both the measured column height of the flow apparatus and by experimental observation of the

volumetric flow rate. To measure volumetric flow, the return line that runs between the flow chamber outlet and the glass column was disconnected and inserted into a collection tube. A stopwatch was used to record the volume collected over a period ranging from 20 to 25 seconds. This was performed three times shortly after setting up the flow apparatus and three times again after the system had been running for over half an hour to ensure that operating temperature had been reached.

Four experiments were performed to evaluate the two in vitro predictions. Each experimental was repeated multiple times. At each iteration, two slides were plated with BAECs expressing wild type lamin and two with cells expressing progerin. In each pair, one slide was used as a control and fixed at the same time as the experimental slide. In the first experiment, cells were placed in the flow chamber under steady flow for four hours. In the second experiment, cells were placed under steady shear for eight hours. In the third and fourth experiments, a P20 pipette tip was used to scratch evenly spaced wounds in the endothelial cell layer spanning the entire slide. One wound was placed lengthwise in the direction of flow while two were placed normal to the direction of flow. In the third experiment, slides thus prepared were subjected to steady shear in the flow chamber for four hours before being allowed to recover for an additional four hours in the incubator before fixation. In the fourth experiment, slides were fixed immediately following eight hours of steady shear. Each of the four experiments were repeated three times except the first experiment which was repeated four times.

2.2.3 Histology

Following each experiment, experimental slides were fixed with 4% PFA simultaneously with control slides after first scoring the downstream end to identify the direction of flow. After washing in PBS, each slide was treated with 0.2% Triton X-100 to render the cells permeable. Slides were washed again and blocked with 1% BSA before incubating overnight with mouse anti-gamma-tubulin (Novus TU-30) at a dilution of 2.1 $\frac{\mu g}{mL}$. Slides were again washed and labeled with donkey anti-mouse AlexaFluor 594 dye (Abcam) at a concentration of 10 $\frac{\mu g}{mL}$. After a minimum incubation period of 4 hours, slides were again washed and

labelled with Hoechst nuclear stain. Samples were stored refrigerated in PBS prior to imaging or in between steps as needed.

2.2.4 Imaging

Cells were imaged using a Leica DFC-350FX microscope. Twelve image locations were selected on each slide by subdividing the slide into six zones and taking two locations per zone. Images were acquired on four channels including phase contrast, fluorescence for Hoechst nuclear stain, fluorescence for ALexaFluor 594, and fluorescence for green fluorescent protein.

2.2.5 Image Processing with Python

Image processing was performed using Python and OpenCV. To assist with file handling, all images were renamed using a consistent format identifying the sample number, experiment type and ID, experimental group, and staining type for each image in the file name. Each sample was represented by four images: phase contrast, Hoechst stain (nucleus), green fluorescent protein stain, and microtubule/actin stain. Desired output from the image processing program included statistical analysis regarding MTOC angular location relative to the nucleus and geometric information about the nucleus. This was achieved by first identifying nuclei, extracting geometric data about the nuclei, identifying microtubule organizing centers, and pairing each nucleus with the correct MTOC.

Nucleus Identification

Nucleus identification was achieved by first performing binary thresholding followed by contour detection to identify each object in the Hoechst nuclear stain image for a given sample. Using built-in OpenCV methods, the convex hull of each contour was subjected to a convexity test. In all or nearly all cases, contours with convexity defects represented regions of overlapping nuclei. Two main approaches were considered to deal with such cases: dropout and segmentation.

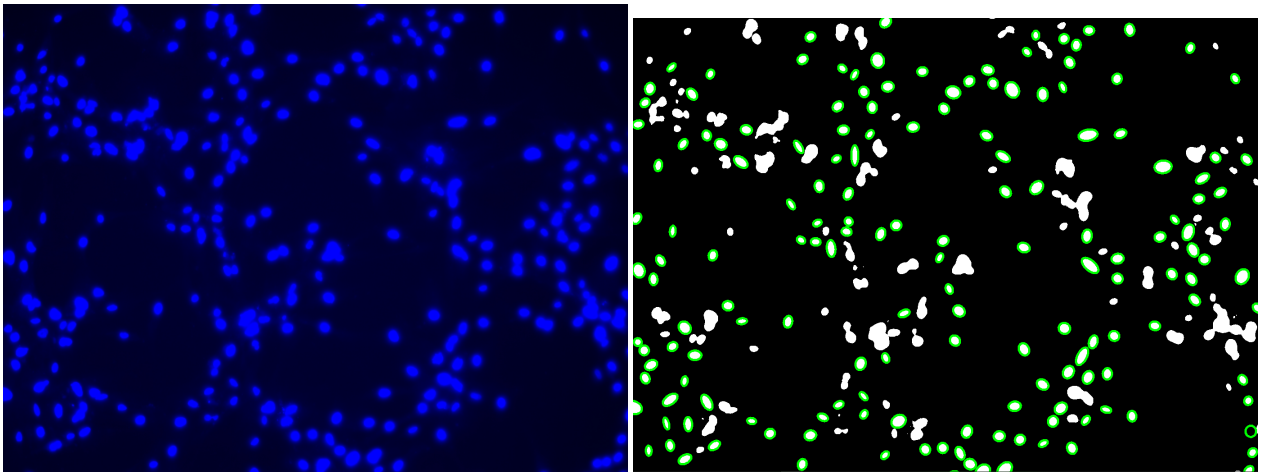

Figure 2.5. Image Processing: Nucleus Detection.
Result of nucleus identification using dropout based on convexity and size. Retained nuclei from original image (left) are outlined in green (right).

The dropout approach was ultimately selected for use in this project. This approach simply discards all questionable nuclei, keeping only the most clearly defined. This was done first by discarding all contours with poor convexity as compared to a threshold value. This still, however, left some irregularly sized contours which were either so small as to be attributable to noise or cellular debris or which were so large as to represent highly convex regions of overlap. The area of each contour was therefore measured and contours lying outside of 20 standard deviations were discarded. Several advantages exist for this approach. In particular, the dropout approach is the simplest to implement, avoids ambiguous cases which could lead lead to uncertainty in the results if retained, and is made practicable by the large amount of data available which leaves sufficient analysis objects even after rigorous criteria are imposed to sift out ambiguous nuclei. Disadvantages for this approach were also considered. Firstly, much data is discarded which could possibly be rescued using a segmentation approach. Secondly, if cell polarization is affected by other cells in close proximity, such affects may be lost to observation when overlapping nuclei are discarded. This may be of especial concern when dealing with the confluent monolayers which are targeted in this particular research. Thirdly, this approach may be expected discard the

most data on cell layers that are highly confluent. In other words, the method struggles most under the best experimental conditions. Despite these disadvantages, however, the advantages were such as to recommend this approach as appropriate under the current conditions.

Image segmentation was also explored before selecting an approach to nucleus identification. The goal of segmentation is to accurately individual nuclei from a cluster of overlapping nuclei. A few of the methods include blob detection, watershed segmentation, and convexity analysis. OpenCV includes built-in methods for blob detection and watershed. Blob detection simply identifies objects but allows sorting based on characteristics such as size and circularity. It is easy to implement but results were not found to be satisfactory for nucleus detection. The watershed algorithm is a well-known approach to this very problem and is used for nucleus detection in ImageJ software. Implementation was more challenging than initially anticipated but it may well be worthwhile to revisit this approach in the future when more time is available. Convexity testing allows a great deal of control and requires the construction of a custom script. In this approach, each contour is tested for convexity defects. If significant defects are found, the contour is split at the point of maximum distance from the convex hull and each daughter contour is tested until all contours pass the convexity test. This method has much to recommend it and should be explored further in future work. Image segmentation has several advantages compared to dropout. It is much more efficient with data by retaining all visible nuclei. This approach would also be expected to better capture any confluency-dependent effects on cell polarization by retaining nuclei in very close proximity. It would also be more versatile, working on both poorly confluent and highly confluent slides. Major disadvantages of this approach are that it is more challenging to implement accurately, but especially that it runs greater risk of inaccurate pairing of nuclei to microtubule organizing centers. For these reasons, further exploration of this approach is reserved to a future project.

MTOC Detection and Pairing

Microtubule organizing centers are usually identified as very small bright spots in the red fluorescent images stained using an anti-gamma-tubulin intermediate. These spots, however, appeared very similar to the far more numerous particles of cellular debris present in fixed slides. In phase contrast images, these debris particles were either very bright or very dark compared to the rest of the image. Images were therefore filtered using binary thresholding to find the intensity extremes in phase contrast images. The contours of the debris particles thus identified were then masked on the corresponding red fluorescent image. After debris removal, binary thresholding was again used to retain only the brightest spots in the red fluorescent image and identify them as MTOCs. Size exclusion based on area was applied to ensure that all detected contours contained no more than a few pixels to further reduce false identifications. For each of the binary thresholding operations, adaptive functions were developed to automate threshold estimation based on the brightness of structures in each image. In the case of debris thresholding, average nuclear brightness was used as the lower threshold while a fractional criterion was applied to the range of brightness values in the image in order to arrive at an upper brightness threshold.

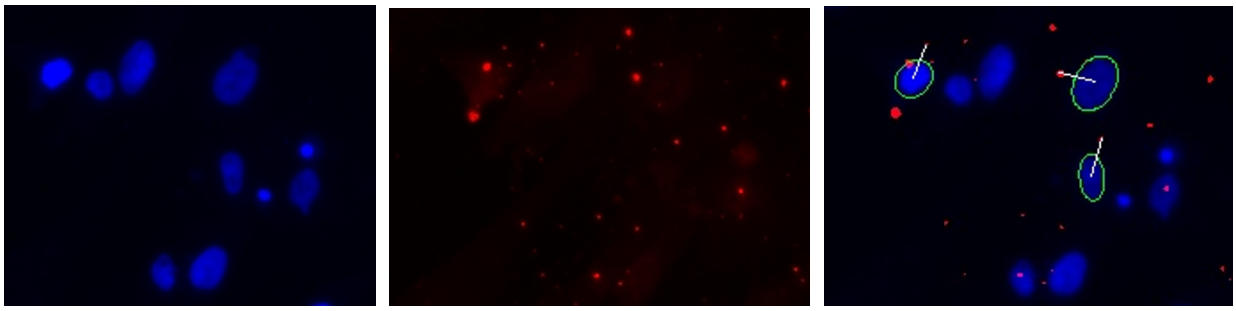

Figure 2.6. Automated nucleus-MTOC pairing.

Once both nuclei and MTOCs have been identified for a particular sample, the MTOCs must be paired with the correct nucleus. Because cell boundary detection using Canny or similar edge detectors did not prove reliable on phase contrast images, these pairs were instead matched using a proximity-based method. Microtubule organizing centers should lie close to the nucleus. Therefore, for each nucleus, a region of influence was defined by scaling

the best-fit ellipse to include the nucleus and a small peripheral boundary. For each nucleus recorded, any MTOCs falling with its region of influence were assigned to that nucleus. The nuclei were then checked and any nuclei which had no paired MTOC or which had more than one paired MTOC were discarded. Furthermore, any MTOCs which were claimed by more than one nucleus were discarded along with the competing nuclei. This process is illustrated in Figure 2.6. The image section is shown in both the channel showing nuclear stain and the channel stained for tubulin. The image on the right shows the nucleus-MTOC pairs selected from this section. Some of the unpaired objects include cellular debris and possible MTOCs lying equidistant between two nuclei. In principle this approach ends up discarding some visual data in exchange for confidence that the data retained are accurately identified and accurately paired. Future work could investigate improvements in edge detection for cell boundary based nucleus-MTOC pairing which could perhaps retain more data without sacrificing accuracy.

3. RESULTS

3.1 In Silico Results

After setting up and running the model as described previously, key results obtained included fluid simulation results from Fluent determining cell loading conditions and mechanical results for model characterization. To this end, several variations on the model were conducted including changes in prestrain for microtubules and knockout of individual parts, namely cytoplasm, microtubules, actin network, and actin fibers, to observe the contribution of each of these parts to the model results. In addition, the in silico predictions were tested by varying MTOC position and nuclear elastic moduli to examine the polarization-dependent stress shielding prediction and the nuclear stiffening prediction respectively.

3.1.1 Fluid Simulation Results

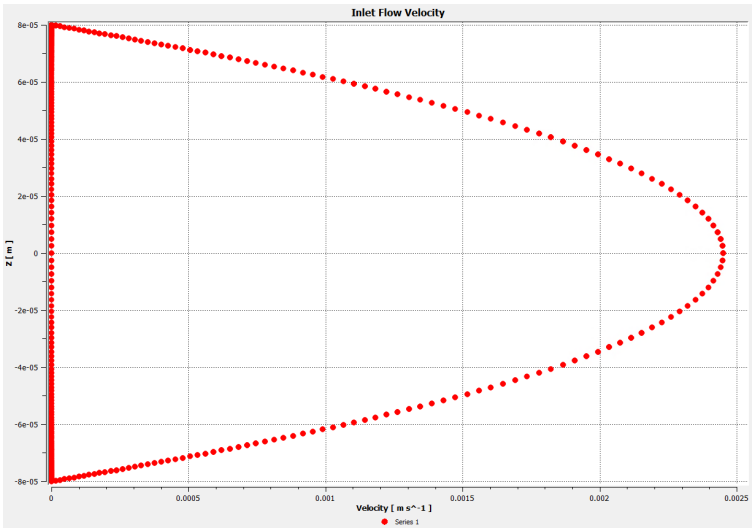

Figure 3.1. Inlet Flow Velocity Profile.

After many adjustments to the Fluent model in terms of flow chamber geometry, mesh, boundary conditions, and initialization conditions, simulation results reasonably close to the calculated target shear stress of 15 $\frac{dynes}{cm^2}$ were obtained. The was accomplished using a density-based solver with a specified Courant number of 0.8. Non-slip boundary conditions were applied to all solid surfaces of the chamber and the inlet velocity was entered as a function of vertical location between the upper and lower surfaces of the chamber. This expression was derived from the Navier-Stokes equation and was successfully implemented as demonstrated in the corresponding figure 3.1.

Both the flow chamber wall shear stress and the stress on the upper cell surface were examined to determine whether they fell within expected limits. As shown here, shear stress on the cell averaged approximately 11 $\frac{dynes}{cm^2}$ with a maximum of 18 $\frac{dynes}{cm^2}$ placing the simulation result near the target shear stress of 15 $\frac{dynes}{cm^2}$. Pressure is also exported from Fluent and combined with shear stress to determine cell loading. For this reason, it was necessary to check for excessive pressures which could dominate the loading profile and prevent solution convergence. As shown in the figure, pressures averaged around 2-3 $\frac{dynes}{cm^2}$ ensuring that cell loading would be dominated by shear stress as desired 3.2. In addition, visual comparison of shear stress and pressure on the cell surface versus on the walls of the flow chamber showed similar average results within an order of magnitude. This suggests that the geometry and mesh were well-configured to prevent sudden changes in behavior in the flow region directly above the cell surface.

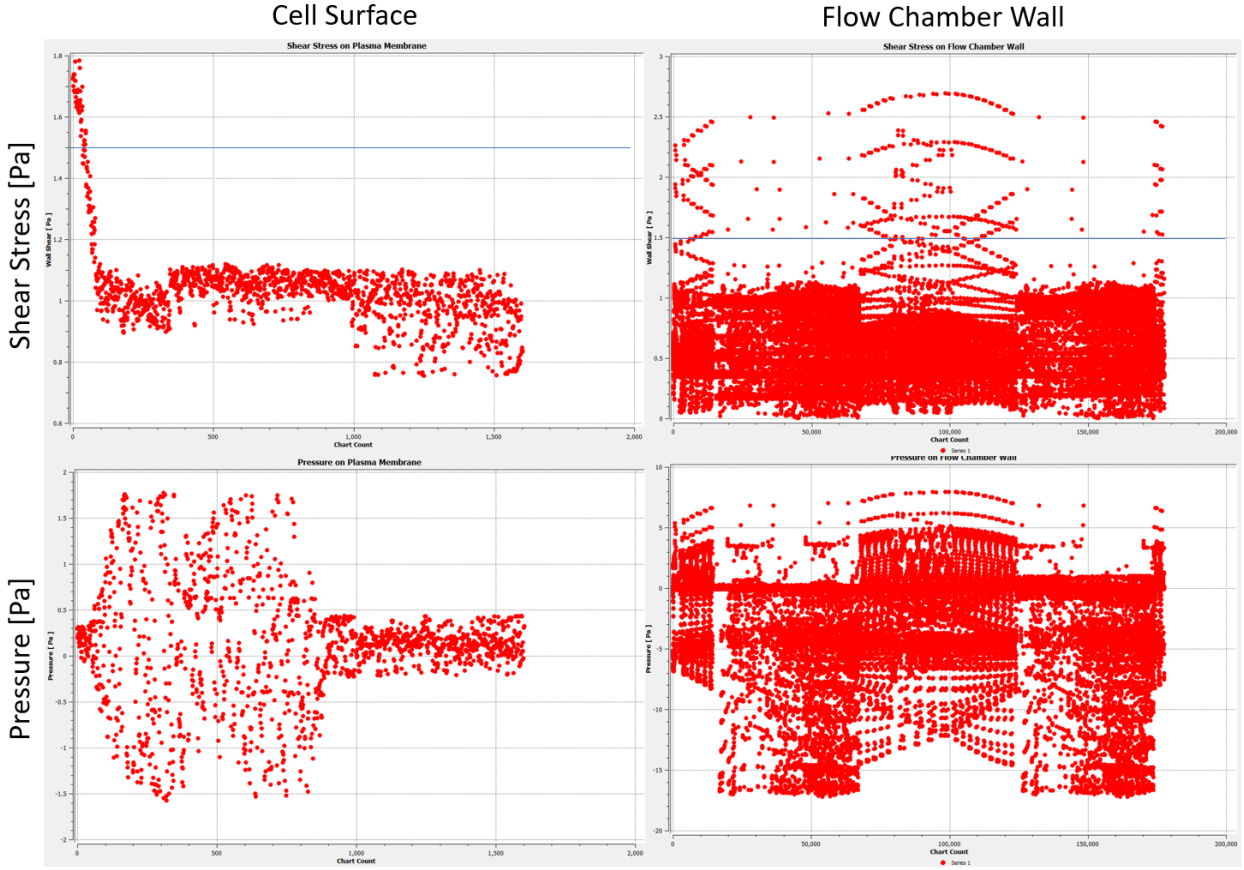

Figure 3.2. Shear Stress and Pressure on Flow Chamber Wall and Cell Membrane.

Upon mapping the load from Fluent into Ansys Mechanical, it was observed that the load was near the expected target with nodal force magnitudes between 13 and 18 $\frac{dynes}{cm^2}$ 3.3. It should be noted that although ANSYS labels imported loads from Fluent as pressures, the load is actually a distribution of nodal loads each of which is the vector sum of shear stress and pressure at that node.

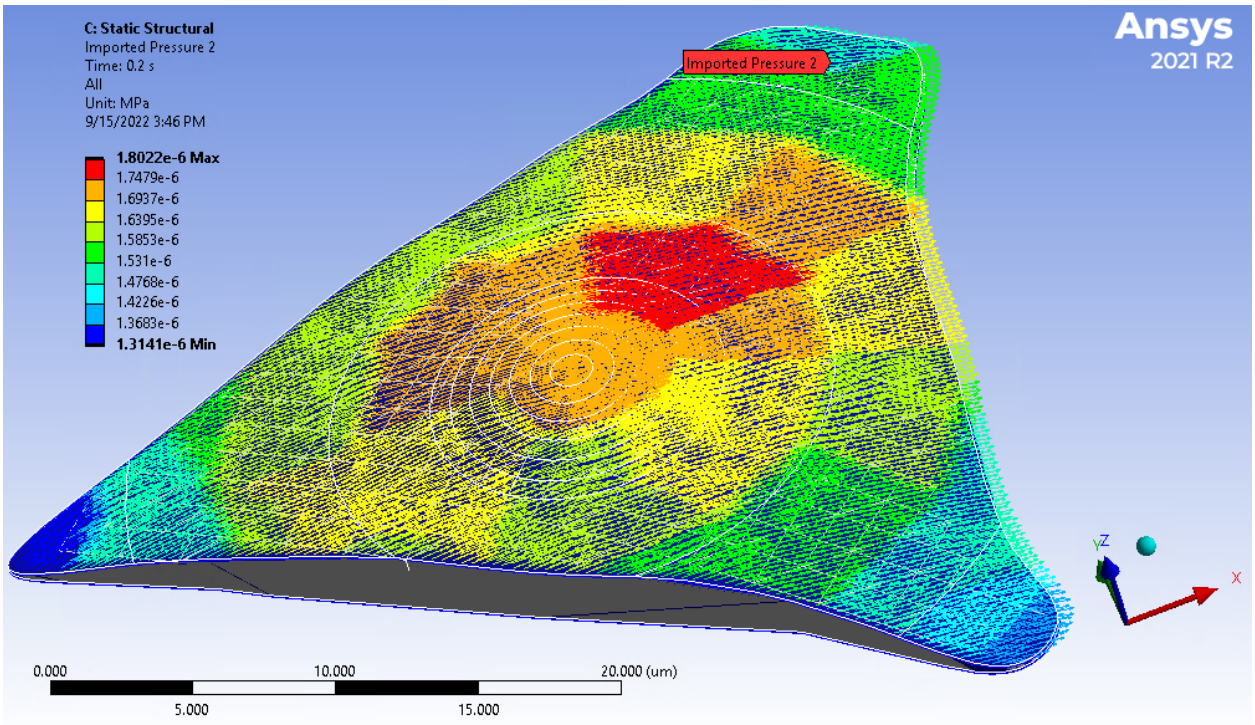

Figure 3.3. Forces Mapped from Fluent Results to Cell Model.

3.1.2 Model Characterization

To better understand the contribution of model components to the overall result, individual parts of the model were removed one at a time and a solution was attempted. Suppression of the cytoplasm, the microtubules, or the actin network resulted in rapid failure of the solution attempt. Removal of the actin filaments tethering the nucleus to the actin network, however, resulted in a nearly 50% decrease in maximum shear stress on the nucleus compared to the same model solution with all bodies unsuppressed. The maximum stress on the nucleus when the actin tethers were present was observed to be 24.6 Pa compared

to only 13.4 Pa when the tethers were suppressed. This suggests that these elements play a key role in force transduction to the nucleus in the current model.

ANSYS allows prestrain to be added to beam elements via an APDL command. Some of the models discussed in the introduction of this thesis found prestrain to be highly significant in tuning the model. To examine whether this was also true of the model here developed a solution was attempted after applying prestrain to beam elements in the degree of 0%, 20%, and 40% prestrain respectively. Because the actin elements were modelled as cable elements for which prestrain is unsupported, prestrain was applied to microtubules (beam elements) only. In all three cases, identical values of 5.05 kPa maximum stress on the plasma membrane and 24.6 Pa maximum stress on the nuclear envelope were returned for each prestrain condition. This suggests that the degree of prestrain applied to the microtubles is irrelevant for this model.

In addition to component removal and prestrain parameterization, the model was checked for reproducibility by solving the model twice using identical settings and also by comparing the results of the model when closely related settings were used such as in the prestrain variation experiment. Model results were initially found to be highly reproducible in the latest model version in contrast to earlier iterations of the model which were not well-conditioned. Fourteen individual solutions taken over a period of about one week showed close agreement in results. The behavior of the solution then changed abruptly with the new behavior remaining consistent over a series of eleven tests over a period of several days. The following results were observed from the most recent set of tests unless otherwise noted.

3.1.3 Cell Polarization

To evaluate the first in silico prediction, that upstream polarization minimizes stress on the nucleus, the MTOC was rotated clockwise to the axis of flow at 0^o, 22.5^o, and 45^o from the upstream and downstream polarization configurations to create six polarization scenarios as shown (Fig. 3.4). It may be noted that the major axis of the nucleus itself was oriented at 45^o to the axis of flow based on the microscope image upon which the cell geometry was modeled 2.2.

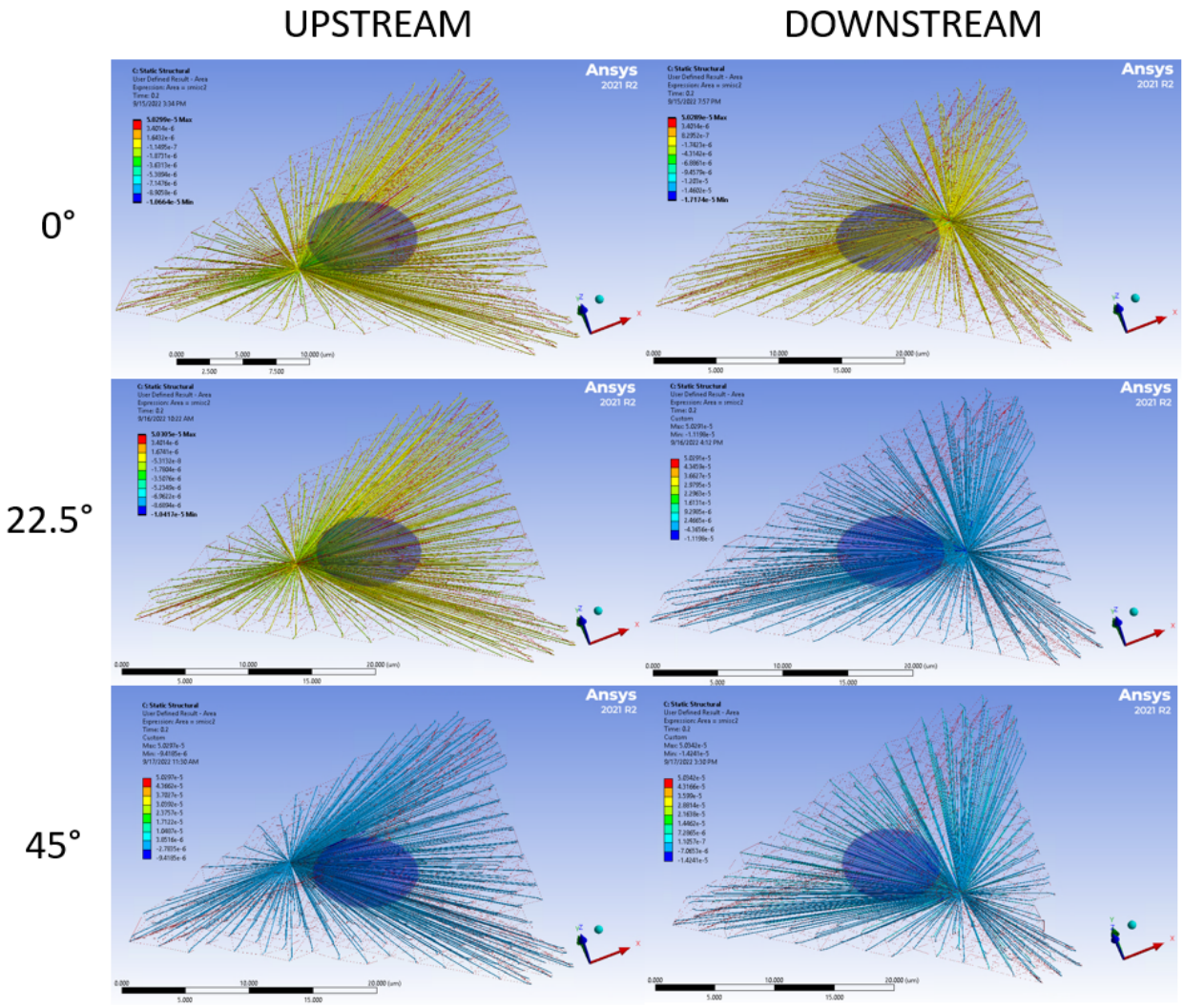

Figure 3.4. MTOC positions used for polarization testing.
Flow direction is positive along the x-axis (red arrow).

Stress concentrations were observed to shift somewhat on the plasma membrane, cytoplasm, and nucleus respectively based on MTOC position. Downstream MTOC position was observed to shift maximum stress on the plasma membrane upstream. General stress regions showed some similarities in all configurations, however. For example, nuclear stress concentrations were observed to occur along the equator parallel to the xy-plane and near points of attachment to actin filaments. This may be illustrated by comparison of the 22.5^o upstream and 22.5^o downstream MTOC positions (Fig. 3.5).

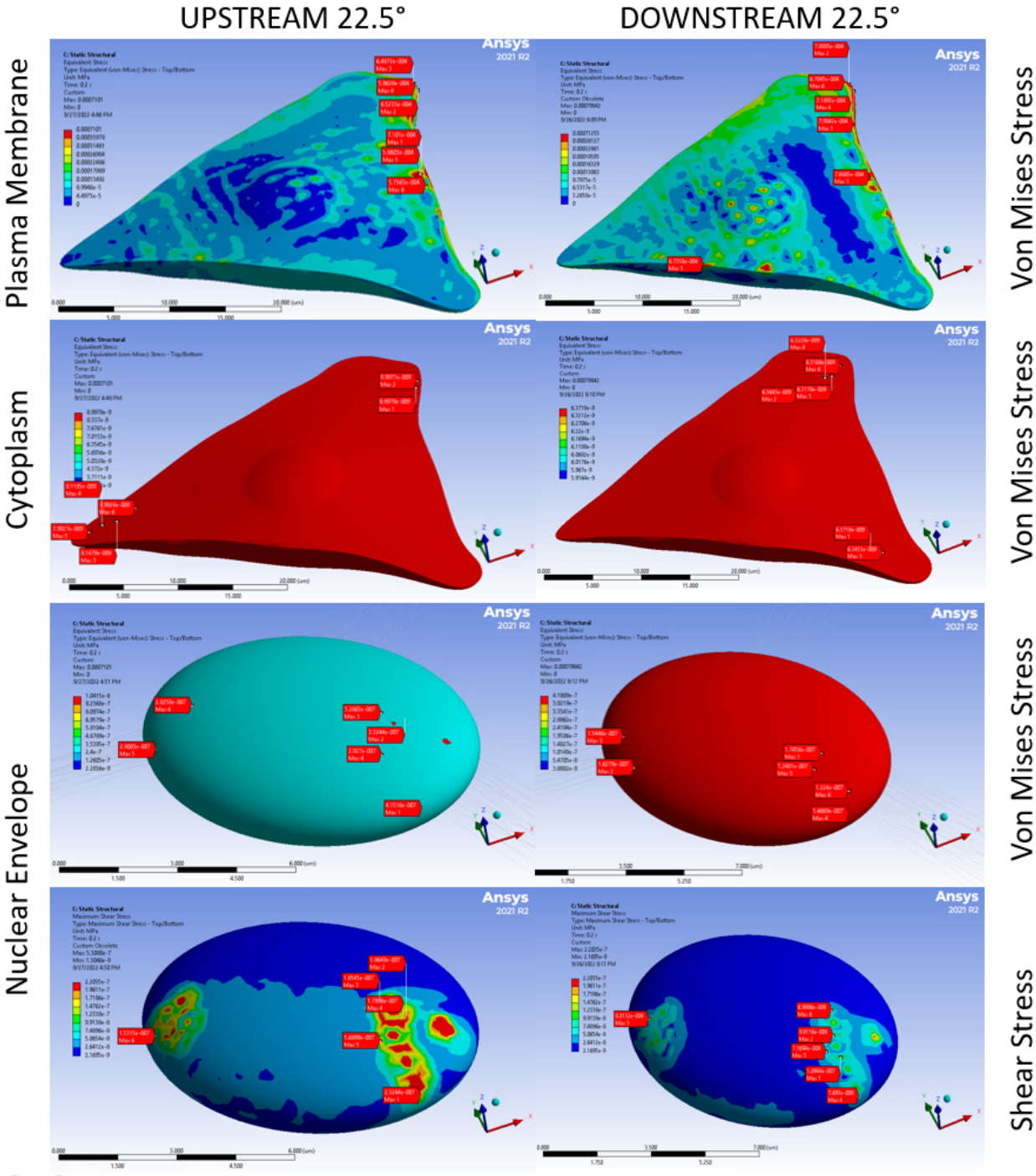

Figure 3.5. Upstream vs. Downstream MTOC results.
Stress concentrations in upstream versus downstream polarization along the axis of flow. Maximum stress nodes are marked with red labels.

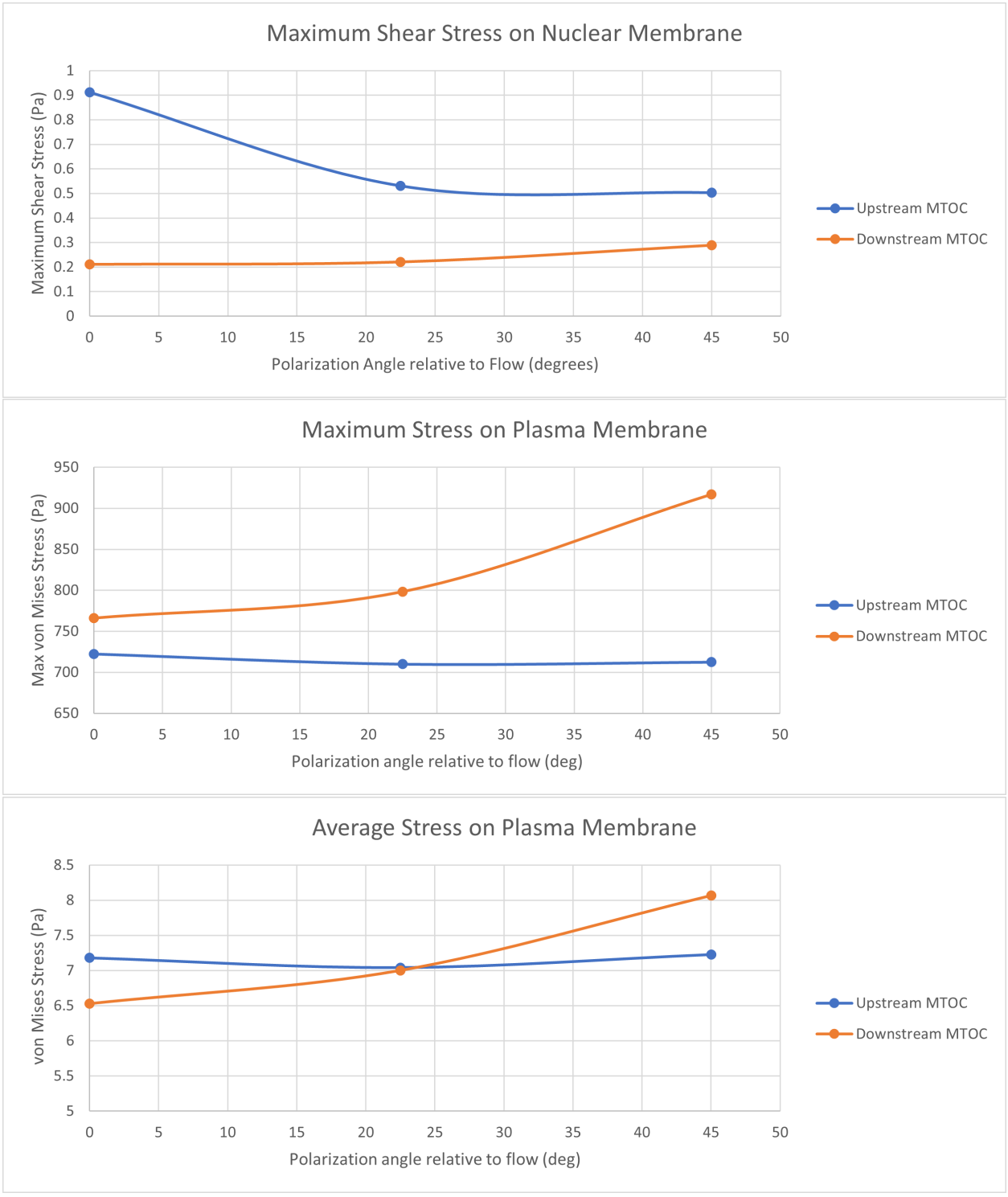

Figure 3.6. Effect of cell polarization on maximum membrane stress. Maximum membrane shear stress on the nuclear membrane (upper), maximum equivalent stress on the plasma membrane (middle), and average equivalent stress on the plasma membrane (lower) at varying cell polarization angles

Maximum stress values on the nucleus were maximized with the cell polarized upstream and minimized when the MTOC was placed downstream of the nucleus. Other orientations yielded intermediate values of maximum stress. Maximum stress concentrations on the plasma membrane, however, showed the opposite trend. Average equivalent stress on the plasma membrane appeared to remain close across all polarization angles as shown in Figure 3.6.

3.1.4 Nuclear Stiffness

As discussed in the background section of this thesis, Booth et al. suggested that the nuclear envelope is stiffened while the nucleoplasm is softened in progerin-expressing cells [19]. In order to see whether such material changes affect stress concentrations at the nucleus, thress scenarios were solved encompassing the range of values suggested by Booth et al. Elastic moduli for the nuclear envelope and nuclear interior are presented in the table below. The series of solutions was solved twice using the same conditions. Both series of results are shown in Table 3.1 and Figure 3.7. Although the magnitudes of the responses differed considerably between the two series, results showed a similar trend. In both series, a strong rise in maximum stress on the nucleus was observed with increasing nuclear membrane stiffness. For the second set of solutions, maximum shear stress on the nuclear membrane is reported along with maximum von Mises stress.

Table 3.1. Nuclear Stiffness Experiment Scenarios.

			Series 1	**Series 2**	
	E_1	E_2	σ_{max1}	σ_{max1}	σ_{max2}
Scenario 1	2500	5000	24.6	0.433	0.242
Scenario 2	5000	2500	43.3	0.684	0.564
Scenario 3	7500	1667	—-	0.901	0.761
Scenario 4	10000	1250	74.6	1.579	0.911

E_1 is the Elastic modulus of the nuclear envelope while E_2 is that of the nucleoplasm. Two series of experiments returned different values for maximum σ_{max1} (von Mises stress) and σ_{max2} (shear stress) on the nuclear membrane.

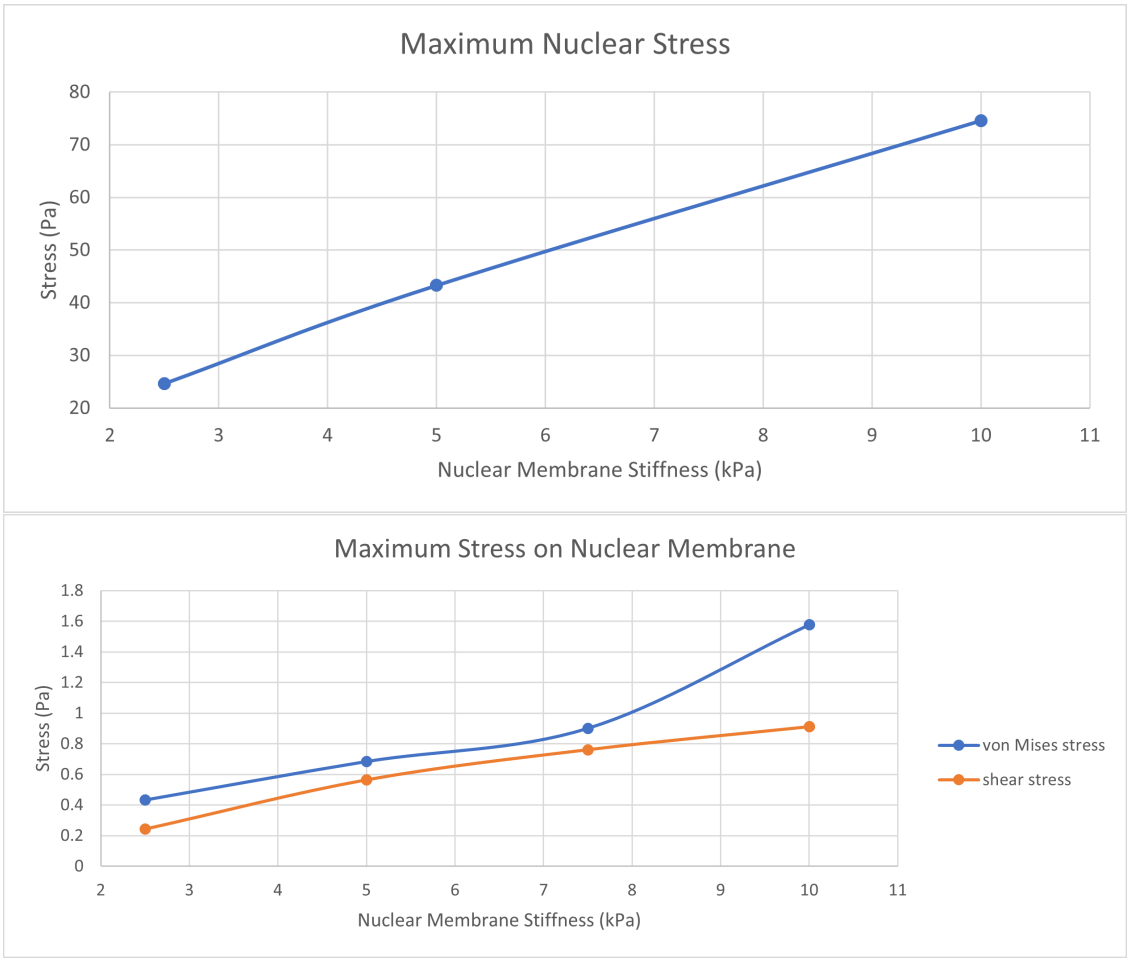

Figure 3.7. Effect of nuclear membrane stiffness on stress concentration. Maximum stress on the nucleus increased proportionally with nuclear membrane stiffness for two series of solutions using identical parameters.

3.2 In Vitro Results

Despite multiple trials for each experiment, none of the slides plated with progerin-expressing cells survived either the 4-hour or the 8-hour steady shear experiments. Although a few slides plated with cells expressing wild type lamin survived, surviving slides were of poor quality (see Fig. 3.8). These slides were nonetheless analyzed using the Python scripts developed for automated image analysis. Results are shown in Table 3.2. Fewer than half of the scratch experiment slides survived and those imaged were of insufficient quality to

evaluate wound recovery. An example of one of the best quality results retrieved from the scratch experiment is shown for illustrative purposes 3.9.

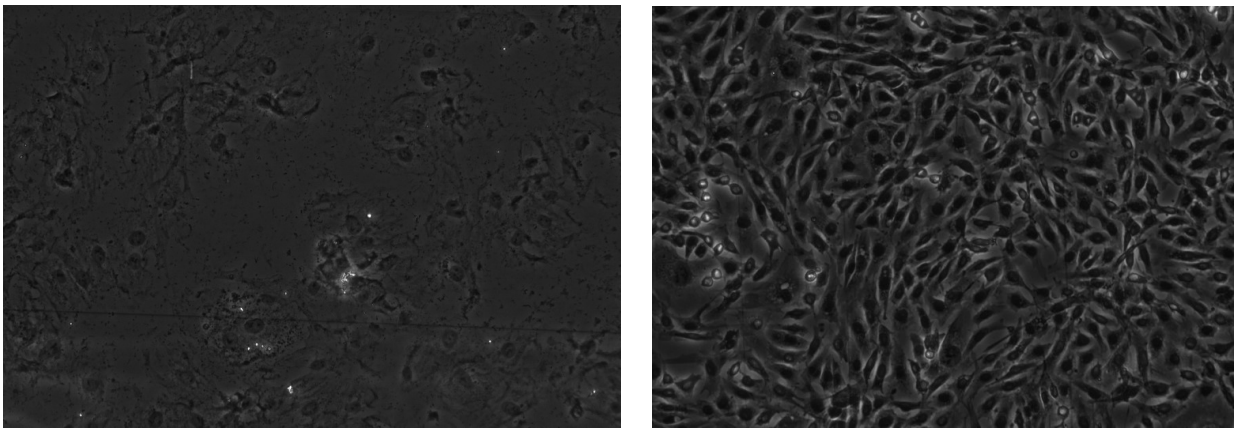

Figure 3.8. Experimental challenges: sample quality comparison.
a typical phase contrast image after a recent flow chamber experiment (left) contrasted with a past experiment performed by former lab member Yizhi Jiang (right)

Table 3.2. Results of steady shear flow experiments.

4-hour Shear Stress

	n_{sets}	n_{pairs}	upstream	downstream	upstream (%)
WT Lamin Control	1	255	135	120	52.9
WT Lamin Shear	2	178	82	96	46.1
Progerin Control	3	451	233	218	51.7
Progerin Shear	0	0	—	—	—

8-hour Shear Stress

WT Lamin Control	1	22	11	11	50.0
WT Lamin Shear	1	238	114	124	47.9
Progerin Control	1	175	83	92	47.4
Progerin Shear	0	0	—	—	—

n_{sets} is the number of surviving slides for each category, n_{pairs} is the total number of nucleus-mtoc pairs identified from images, and mtoc position is upstream or downstream relative to the nucleus. No progerin-expressing cell slides survived.

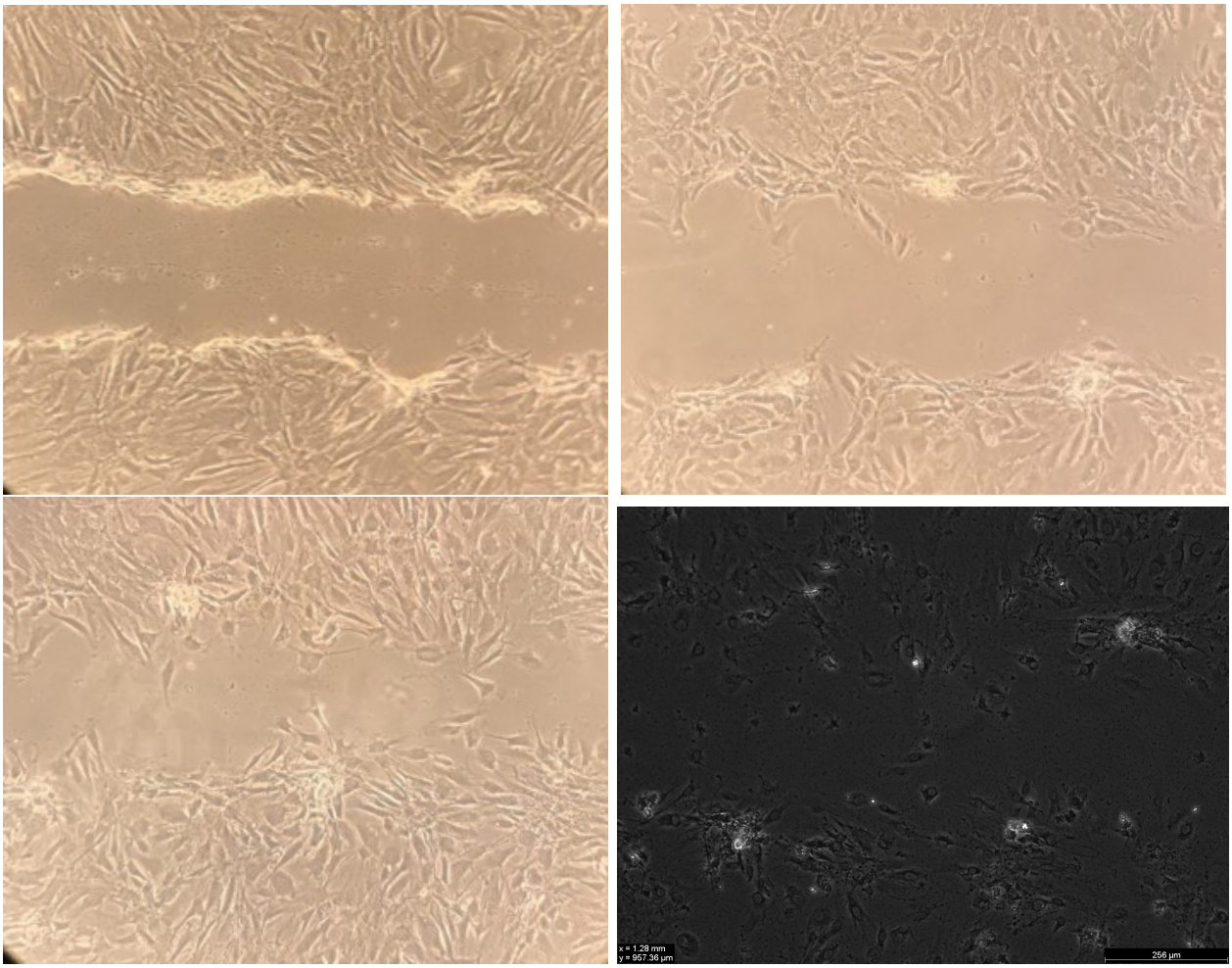

Figure 3.9. Experimental challenges: sample deterioration.
4-hour shear followed by 4-hour recovery scratch assay shown immediately before shear (top left), immediately after removal from shear (top right), immediately before fixation (bottom left), and after preparation for imaging (bottom right)

4. DISCUSSION

4.1 Fluent Results

The fluid simulation results here presented are the result of many days of tuning through trial and error. Small changes to boundary conditions and initialization conditions may cause results to vary greatly. Although a suitable configuration of Fluent was found which returned a reasonable range of shear stress, some questions remain. Average pressure at the cell surface was a low positive value as expected, but many points of negative pressure were observed both on the cell surface and on the flow chamber walls (Figure 3.2). The meaning of this remains unclear and warrants investigation. The inlet flow velocity demonstrated the expected parabolic profile, but data points of zero velocity were also observed for each z-coordinate (Figure 3.1). Zero flow profile plots were also observe in the interior of the flow chamber. The reason for this data outcome is ambiguous. It was also noted that reasonable solutions of the Fluent model could be found only using the density-based solver and not using the pressure-based solver although both methods ought to return similar results. This may be due to the very small scale of the dimensions and magnitudes for pressure and velocity involved in the simulation. While the simulation appears to produce reliable results within expected ranges where cell loading is concerned, future work should nonetheless rigorously evaluate the stability of the current solution.

4.2 Model Characterization Results

A key consideration in finite element modeling is the stability of results. In particular, it is common practice to repeat a solution using various mesh settings to ensure that the model results are not an exotic accident of meshing. Unfortunately, this model did not lend itself well to such an approach. The geometries of several bodies were not easily meshed. This was particularly true of the cytoplasm. Mesh settings resulting in acceptable element quality were difficult to achieve making it a challenge to build and test multiple meshes in the time available. Although the current version of the model initially appeared to be stable, model behavior was observed to change suddenly as previously mentioned. This change was evident

both in the values of maximum shear stresses (up to 100X lower) and in the distribution pattern of stresses on the plasma membrane. Following this change, results have have once again been consistent across multiple simulations. Because no model settings or parameters were altered between these two sets of results, the reason for this difference remains unclear at the present time. The behavior change coincided with a clearing and regeneration of the model mesh. The behavioral change also coincided with several days of inactivity raising the possibility that some program-controlled memory cache was cleared. In the most recent set of simulations, however, the mesh was cleared and regenerated between each solution with no significant resulting changes observed in model behavior. The lower numerical results for stress response also appear more reasonable since the applied load did not exceed 1.8 Pa. For these reasons, the most recent set of solutions appears to be the more reliable and was therefore selected for inclusion in the Results section of this thesis. Future work should nevertheless investigate this question further and make confirmation of model stability a top priority. In particular, other mesh settings should be explored to confirm model stability. Until this question has been resolved, simulation results should be regarded with caution.

Despite these reservations, many similarities were observed between the two sets of simulations. Indeed, most trends remained the same. The greatest differences were that the stress magnitudes were decreased by 1-2 orders of magnitude in the most recent simulations and that regions of highest stress response on the plasma membrane were significantly shifted relative to the previous results. Fluent simulation results and imported nodal force mapping, however, were not affected by the behavioral change. Furthermore, the model has made remarkable recent progress in the area of convergence. Previous model versions demonstrated frequent solution bisections and either failed to converge or required solver run times around 36 hours on 20 cores. In contrast, the present model version exhibits few solution bisections and requires 2-3 hours to solve on 8 cores suggesting a better-conditioned model.

The finding that prestrain on microtubule structures did not affect stress distribution on cell membranes was not expected but may be due to the selection of line body element types. Cable elements such as those used for actin structures in this model do not support application of prestrain while prestrain may not have a significant effect on beam elements such as those used to represent microtubules unless significant bending moments are present.

Had prestrain on actin filaments been included by switching actin line bodies from cables to LINK180, prestrain would likely have increased bending moments on microtubules through their interactions with beam ends. This question could be investigated in future work.

The key finding of body elimination experiments was that direct actin connections to the nucleus played a key role in force transduction to the nucleus. In other words, significant force transduction occurs along the cytoskeleton as well as through direct forces exerted by the cytoplasm and plasma membrane in this model. This is significant because the actin cortex is reported to form connections with LINC complexes in the nuclear envelope. This reality has been represented in very simplified fashion through the presence of a few tethering cables in the finite element model. This finding suggests that future work ought to focus on refining this particular element of model design in light of its key importance as a force transduction mechanism.

Regarding the role of cytoplasm in force transduction, it may be inquired whether the contribution of this ultra-low stiffness body to force transduction justifies the high computational demands of its presence in the model. Although the solver quickly failed with this body suppressed in the current model version, previous iterations found that the cytoplasm body significantly contributed to force transduction. This is likely a attributable to the high bulk modulus assigned to the material allowing transfer of pressure. Although the cytoplasm was found to be the sole driver of the model's high computational demands in previous iterations, it appears to be an essential component of the model.

4.3 First Computational Objective

It was predicted that upstream polarization minimizes stress on the nucleus. Results demonstrate that this prediction should be rejected. This result was unexpected and could shed light on the disparity between in vitro results reported by various groups. This prediction was predicated on the assumption that direct forces dominate cell surface loading under hemodynamic flow. Contrary to this expectation, the fluid simulation portion of this model found that loading was maximized downstream of the nucleus suggesting that drag forces may dominate cell surface loading. It should be noted that region of maximum loading was

found to be slightly off the axis of flow (Figure 3.3). Comparison to the nuclear orientation which was rotated 45^o relative to the axis of flow shows that the region of maximum load coincides with the region that would be expected to experience the greatest drag force. The stress response in the mechanical portion of the simulation, however, still upheld the idea that MTOC position places an important role in stress management and that maximum stresses on the nucleus were minimized when the MTOC was placed near the position of maximal loading. In addition to maximum equivalent stress, maximum shear stress on the nucleus was also decreased when the MTOC was placed in the downstream position. Results on the plasma membrane were more nuanced. In the most recent set of simulations, maximum stress on the plasma membrane was actually increased when the MTOC was placed downstream of the nucleus while average stresses remained relatively similar at all orientations. Notably, stress concentrations were shifted away from the downstream side of the cell when the MTOC was polarized downstream.

If the simulation here presented has accurately captured the behavior of real systems, this result could provide evidence for the possible participation of MTOC position in stress signal management while also suggesting a plausible mechanical explanation for variations in cell polarization. Because the nucleus appears to dominate the protrusion of the endothelial cell above the monolayer, the nucleus size, orientation relative to the axis of flow, and proximity to nearby cells would dictate the drag forces acting on the cell surface. Furthermore, the mechanical simulation results demonstrate that stress management is not a binary proposition of upstream versus downstream MTOC placement, but that maximal stresses on the nucleus may be modulated by varying the MTOC position. Because nucleus size and rotation vary somewhat from cell to cell within the same monolayer, drag force will necessarily vary from cell to cell. Although nuclear size and rotation may follow a trend at the population level in many cases, it would not be surprising to find this trend to vary based on factors such as species, age, and environment. Cell polarization might therefore vary accordingly in order to avoid excessive or insufficient stimulation from nuclear stresses. While this explanation remains an informed conjecture at best, it could provide a important shift in our understanding of endothelial cell loading if confirmed. This conjecture could be tested by image

analysis of previously reported data to observe whether MTOC position correlates to nucleus size and orientation as indicators of drag force magnitude and concentration.

4.4 Second Computational Objective

It was predicted that nuclear envelope stiffening causes increased reaction stress at the nucleus. Simulation results strongly supported this prediction. Despite the wide gap in magnitudes recorded by the two series of simulations, the trend remained starkly similar in both. This finding is of primary significance in that it suggests a direct mechanistic link for dysregulation of gene expression in progerin-expressing cells. As previously discussed, lamin is the dominant structural protein composing the nuclear membrane. Partial or complete replacement of wild type lamin with progerin as occurs in HGPS and to some degree in the normal aging process alters the stiffness of the nuclear components. Simulation results demonstrate that such a change in stiffness has the potential to dramatically alter force transduction to the nucleus. Such alterations would be expected to affect gene expression. Because of the potential importance of this finding, future iterations of the finite element model should check whether this result consistently appears as the model undergoes further refinement.

4.5 In Vitro Results

In vitro experiments did not directly produce usable results due to issues with confluence and survivability of plated slides. The reasons for poor experimental outcomes are not immediately clear. Both control slides and slides placed under shear were subject to cell deterioration despite exhibiting healthy appearances prior to cell fixation with paraformaldehyde. In addition, some slides deteriorated while other slides fixed at the same time did not. Moreover, of those slides which survived, MTOCs were difficult to identify with any certainty and cell confluency was generally inadequate. Both of these setbacks were likely due to personal inexperience going into these experiments. Scratch assays did not show any clear cell layer recovery. This could be due to insufficient cell layer confluency at the start of the shear experiment or to excessive loss of cells under shear. Because the experiments did not

produce quality results, the in vitro predictions could not be evaluated. In light of simulation results, however, revisions to these predictions should be considered in future work.

The cause of the unsatisfactory outcomes for flow experiments is not clear. The elevated failure rate for experimental slides compared to controls suggests that there may have been an issue with the flow setup. To gauge this possibility, flow rate was observed downstream of the flow chamber as described in the Methods section and inserted into the shear stress equation to estimate shear stress in the chamber. This flow rate was observed to be $0.533 \pm 0.01 \frac{mL}{s}$ after reaching operating temperature yielding a calculated shear stress of $30.6 \frac{dynes}{cm^2}$. This is significantly lower than the calculated estimate of $39 \frac{dynes}{cm^2}$ using column height alone, perhaps due to the resistance of the small-diameter tubing used to connect the flow chamber to the fluid column. It remains, however, well above the target $15 \frac{dynes}{cm^2}$ high shear stress condition. These calculations are dependent upon the accuracy of cell medium viscosity reported by another group [33]. While excessive shear could partially explain attrition, significant losses were also seen among control slides. Survival of some slides and failure of others fixed simultaneously suggests that cell fixation did not likely cause the issue. Post-experiment handling may have been the main contributor to losses. This effect is clearly seen in bright-field images of a slide taken during scratch experiments which shows substantial deterioration following staining and storage despite good confluency at the start of the experiment 3.9. These images suggest that losses occurred mainly during handling, staining, or storage.

Despite the lack of direct results from the in vitro experiments, the development of specialized Python tools for automating image processing may be regarded as a significant outcome which may prove useful in future work. Provisional results on cell orientation reported by the current scripts should not be taken as authoritative since they could not be absolutely confirmed by manual inspection. Individual MTOCs identified by the software, however, appeared plausible and the scripts were observed to function as desired. Once properly calibrated these scripts could greatly reduce time and effort previously required for results analysis while avoiding human inconsistency. Future work should seek out standard test images with clearly identifiable MTOCs. Such images could then be used to calibrate the Python script parameters to ensure greater accuracy of results. Future work should also combine the various Python scripts used in this project into a single program with a

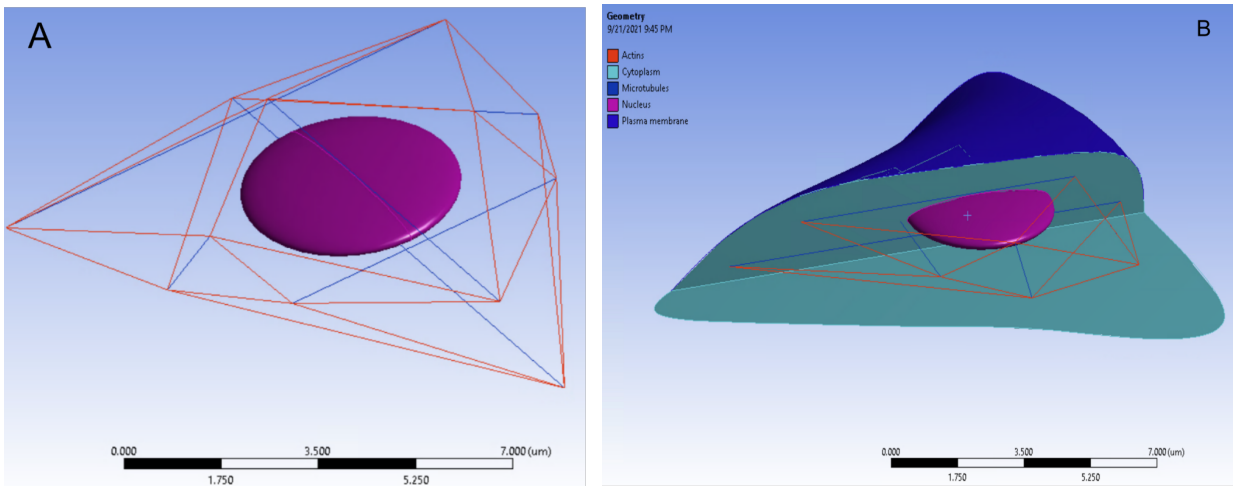

Figure 4.1. Original finite element model.
Tensegrity structure (A) and cross-sectional view (B) of finite element model design at the beginning of this thesis work [35].

graphical user interface for parameter adjustment to make these tools more accessible and user-friendly.

4.6 Model Progress

The work presented in this thesis represents strong progress in model development. At the beginning of this work, the latest model iteration consisted of a floating tensegrity structure surrounding a solid circular nucleus embedded within a bulky cytoplasm (Figure 4.1). The tensegrity structure contained 6 microtubules and 24 actin filaments, both modeled as truss links (LINK180). The cytoplasm was vertically shaped by four arbitrary freehand spline curves. There was no common node for compressive tensegrity elements to represent the microtubule organizing center and the model solution would not converge. Cell geometry updates had to be made manually in DesignModeler or an external CAD program.

In the course of the work presented in this thesis, the model has increased greatly in complexity, utility, and ease of use. As of the time of this thesis publication, the latest model iteration has 392 microtubules modeled as beam elements, 1038 actin network fibrils modeled as cable elements, and 72 nuclear actin filaments modeled as cable elements. These

tensegrity components have been joined in a way that reflects cell geometry more accurately than the preceding model including features to represent the MTOC and the actin mesh network. The vertical cell shape has been defined mathematically to mimic the profile of live endothelial cells. The deeply embedded solid nucleus has been replaced by a prominent ellipsoid modeled as a thin shell filled with hydrostatic fluid facilitating more realistic force transduction, analysis of the nuclear membrane as a distinct body, and decoupling of the material properties of the nuclear envelope and the nucleoplasm for more advanced study. Additionally, convergence issues which plagued most model iterations have been resolved in the latest version. Repeated testing has shown that model solutions now dependably converge without returning solver errors or excessive bisections. The utility of the model has further been demonstrated by nuclear stress experiments as reported in the previous section.

Increases in model complexity and utility have been supported by the creation of tools which greatly improve ease of use for future edits to the model. A simple graphical input tool allows the shape of the cell base and the position of the nucleus to be quickly updated to model a new endothelial cell from an image. The processes of cytoskeletal component generation have been defined algorithmically so that the tensegrity structures of the model adjust automatically to changes in the base profile shape upon regeneration of the coordinates files. The complexity of the cytoskeleton can also be adjusted by changing a single variable representing cytoskeletal element density. New coordinates files can be easily imported into the existing model, allowing the new geometry to be quickly implemented without recreating the model in ANSYS.

4.7 Future Directions

While great progress has been made in the course of this work, there are many areas which would benefit greatly from further refinement. Model conditioning should be thoroughly tested by adjusting mesh settings in ANSYS Mechanical and checking for significant changes in solution results. The Fluent module results should be similarly tested by observing the effects of small changes to input parameters to solver output. The scale of the model should also be examined. While finite element analysis results are theoretically scale agnostic, very

small numerical values may lead to computational errors. The model ought therefore to be recreated at a larger scale for comparison of results to the original micrometer-scale model.

This work found that force transduction to the nuclear membrane is significantly affected by direct nuclear attachments to the cytoskeleton. The nuclear actin filaments used in the present model should therefore be further refined to more appropriately reflect the geometric connections between the nuclear envelope and the actin cortex of the cell. In addition, future work could examine the feasibility of using non-linear materials for cellular components. Multi-cell models could also be constructed to examine effects of nearby cell geometries in cell surface loading due to fluid shear.

A collection of Python scripts was created to automate cell feature generation and image processing. In their current state, however, use of these tools requires some experience with Python and significant familiarity with the project. The scripts also are somewhat decentralized and may have passages of unused code leftover from previous iterations. The scripts ought therefore to be cleaned up and combined into a single project. Development towards parameter management using TOML files and a comprehensive graphical user interface for parameter input has been started but has yet to be completed. Such work would make the Python tools much more straightforward for new users. There are also many features in the code which could be refined or expanded in future work. Particular areas for future refinement include better calibration for image processing tools, image segmentation for improved nucleus detection, and improvement of the MTOC-detection algorithm. Predefined cell shapes could also be included as options in addition to generation of custom shapes from images. A more ambitious goal for future development might be to run ANSYS in batch mode from the same user interface, allowing all aspects of cell simulation from defining the cell geometry to solving the model to be handled from a single graphical user interface. An alternative goal for the future of this project might be to develop a custom finite analysis tool using open-source Python packages. This approach would circumvent the license access issues frequently encountered in the use of shared ANSYS resources and allow the model to be distributed to a wider academic audience.

5. CONCLUSION

Laminopathies such as Hutchinson-Gilford progeria syndrome are a family of genetic diseases in which a mutation causes aberrant lamin protein expression. One particular hallmark of HGPS is advanced cardiovascular aging leading to early mortality. Because lamin is the primary structural protein of the nuclear envelope, the altered structure of the lamin protein alters the mechanical properties of the nucleus. The exact mechanism by which lamin mutation leads to advanced cardiovascular aging remains incompletely understood although several possible mechanisms have been suggested. It has been proposed that altered nuclear mechanical properties in progerin-expressing arterial endothelial cells cause pathological changes to gene expression by interfering with the mechanodransduction of hemodynamic shear stresses to the nucleus.

Construction of a finite element model of the endothelial cell could serve as a valuable tool for exploring this proposition. Existing published models are limited, however, in a number of ways. While hybrid models combining tensegrity and continuum model concepts have made significant progress, published models have been limited to regular geometries with an embedded nucleus. This work presents a more advanced finite element model based on the irregular geometry of an imaged endothelial cell with a vertical profile dominated by a protruding cell nucleus in keeping with published observations on endothelial cell surface topology. Development of supporting scripts to automate generation of construction points also supports future investigation by allowing rapid adaptation of model concepts to other cell geometries with full control over the density of cytoskeletal networks.

Simulations using the model here presented revealed three key findings. Firstly, the fluid simulation showed that drag forces were dominant in cell surface loading. This was a direct consequence of constructing the vertical profile of the cell with a prominent raised nucleus and may shed light on the mechanism of fluid-cell interaction at the arterial wall. Secondly, stress magnitudes on the plasma membrane and, more importantly, on the nuclear membrane could be modulated by adjusting the angular position of the MTOC relative to the nucleus. This supports the idea that cell polarization plays a role in stress sensing in arterial cells and leads to speculation that cells could use this effect to fine tune nuclear shear sensing. Downstream

MTOC positions were observed to reduce membrane stresses compared to upstream MTOC positions. This effect appears to be a direct result of drag force dominance in cell loading and therefore may not be predicted by other existing models which embed the nucleus deep within a regular dome structure. Finally, nuclear stiffness experiments in the simulation predicted that alterations to the mechanical properties of the cell nucleus on a scale reported in live nuclei would lead to dramatic changes in maximum membrane stresses on the nucleus. This result supports the proposed idea of a direct mechanism for altered gene expression in progerin-expressing arterial cells caused by altered nuclear stress sensing in response to hemodynamic shear.

While this work presents significant foundational progress for an improved finite element model of nuclear stress sensing, many limitations remain to be addressed by future work. Firstly, the sudden behavior change in the model described previously means that model stability remains a concern of first importance. Secondly, fluid simulation solutions were found to be highly sensitive to changes in simulation settings and should be further explored before great confidence is placed in simulation results. Thirdly, the direct connections between the cytoskeleton and the nucleus were represented in a simplified manner by a few cable structures. Results showed that these structures play a greater role in force transduction than initially anticipated. The modeling of these particular connections should therefore be reevaluated with greater care. Fourthly, in vitro cell studies performed did not produce usable results and therefore could not be used to corroborate simulation findings. While the ability of flow experiments to provide reliable corroboration unclouded by alternative explanations for cell behavior may be limited, these experiments should be repeated in the future. Finally, the image processing script for nucleus-MTOC pairing would benefit from further calibration using cleaner cell images than those available at the time of evaluation.

While acknowledging the above limitations, it is believed that this work represents an important step forward for exploration of mechanical aspects of nuclear sensing of hemodynamic shear stress in endothelial cells. While caution is advised, preliminary simulation results point to a couple of exciting discoveries which could shed light on the mechanistic link between laminopathy and arterial disease. It is hoped that the tools developed and presented herein may lay the groundwork for further refinement and future discoveries.

LIST OF REFERENCES

[1] P. Libby, P. M. Ridker, and G. K. Hansson, "Progress and challenges in translating the biology of atherosclerosis," *Nature*, vol. 473, no. 7347, pp. 317–25, 2011, ISSN: 1476-4687 (Electronic) 0028-0836 (Linking). DOI: 10.1038/nature10146. [Online]. Available: https://www.ncbi.nlm.nih.gov/pubmed/21593864.

[2] A. M. Malek, S. L. Alper, and S. Izumo, "Hemodynamic shear stress and its role in atherosclerosis," *JAMA*, vol. 282, no. 21, pp. 2035–42, 1999, ISSN: 0098-7484 (Print) 0098-7484 (Linking). DOI: 10.1001/jama.282.21.2035. [Online]. Available: https://www.ncbi.nlm.nih.gov/pubmed/10591386.

[3] S. Chien, "Mechanotransduction and endothelial cell homeostasis: The wisdom of the cell," *Am J Physiol Heart Circ Physiol*, vol. 292, no. 3, H1209–24, 2007, ISSN: 0363-6135 (Print) 0363-6135 (Linking). DOI: 10.1152/ajpheart.01047.2006. [Online]. Available: https://www.ncbi.nlm.nih.gov/pubmed/17098825.

[4] J. M. Phillip, I. Aifuwa, J. Walston, and D. Wirtz, "The mechanobiology of aging," *Annu Rev Biomed Eng*, vol. 17, pp. 113–141, 2015, ISSN: 1545-4274 (Electronic) 1523-9829 (Linking). DOI: 10.1146/annurev-bioeng-071114-040829. [Online]. Available: https://www.ncbi.nlm.nih.gov/pubmed/26643020.

[5] J. Lammerding, P. C. Schulze, T. Takahashi, *et al.*, "Lamin a/c deficiency causes defective nuclear mechanics and mechanotransduction," *J Clin Invest*, vol. 113, no. 3, pp. 370–8, 2004, ISSN: 0021-9738 (Print) 0021-9738 (Linking). DOI: 10.1172/JCI19670. [Online]. Available: https://www.ncbi.nlm.nih.gov/pubmed/14755334.

[6] J. A. Frangos, L. V. McIntire, and S. G. Eskin, "Shear stress induced stimulation of mammalian cell metabolism," *Biotechnol Bioeng*, vol. 32, no. 8, pp. 1053–60, 1988, ISSN: 0006-3592 (Print) 0006-3592 (Linking). DOI: 10.1002/bit.260320812. [Online]. Available: https://www.ncbi.nlm.nih.gov/pubmed/18587822.

[7] C. G. Galbraith, R. Skalak, and S. Chien, "Shear stress induces spatial reorganization of the endothelial cell cytoskeleton," *Cell Motil Cytoskeleton*, vol. 40, no. 4, pp. 317–30, 1998, ISSN: 0886-1544 (Print) 0886-1544 (Linking). DOI: 10.1002/(SICI)1097-0169(1998)40:4<317::AID-CM1>3.0.CO;2-8. [Online]. Available: https://www.ncbi.nlm.nih.gov/pubmed/9712262.

[8] S. Li, N. F. Huang, and S. Hsu, "Mechanotransduction in endothelial cell migration," *J Cell Biochem*, vol. 96, no. 6, pp. 1110–26, 2005, ISSN: 0730-2312 (Print) 0730-2312 (Linking). DOI: 10.1002/jcb.20614. [Online]. Available: https://www.ncbi.nlm.nih.gov/pubmed/16167340.

[9] S. McCue, D. Dajnowiec, F. Xu, M. Zhang, M. R. Jackson, and B. L. Langille, "Shear stress regulates forward and reverse planar cell polarity of vascular endothelium in vivo and in vitro," *Circ Res*, vol. 98, no. 7, pp. 939–46, 2006, ISSN: 1524-4571 (Electronic) 0009-7330 (Linking). DOI: 10.1161/01.RES.0000216595.15868.55. [Online]. Available: https://www.ncbi.nlm.nih.gov/pubmed/16527990.

[10] E. Tzima, W. B. Kiosses, M. A. del Pozo, and M. A. Schwartz, "Localized cdc42 activation, detected using a novel assay, mediates microtubule organizing center positioning in endothelial cells in response to fluid shear stress," *J Biol Chem*, vol. 278, no. 33, pp. 31 020–3, 2003, ISSN: 0021-9258 (Print) 0021-9258 (Linking). DOI: 10.1074/jbc.M301179200. [Online]. Available: https://www.ncbi.nlm.nih.gov/pubmed/12754216.

[11] E. Tkachenko, E. Gutierrez, S. K. Saikin, *et al.*, "The nucleus of endothelial cell as a sensor of blood flow direction," *Biol Open*, vol. 2, no. 10, pp. 1007–12, 2013, ISSN: 2046-6390 (Print) 2046-6390 (Linking). DOI: 10.1242/bio.20134622. [Online]. Available: https://www.ncbi.nlm.nih.gov/pubmed/24167710.

[12] A. F. Palazzo, H. L. Joseph, Y. J. Chen, *et al.*, "Cdc42, dynein, and dynactin regulate mtoc reorientation independent of rho-regulated microtubule stabilization," *Curr Biol*, vol. 11, no. 19, pp. 1536–41, 2001, ISSN: 0960-9822 (Print) 0960-9822 (Linking). DOI: 10.1016/s0960-9822(01)00475-4. [Online]. Available: https://www.ncbi.nlm.nih.gov/pubmed/11591323.

[13] A. Gojova and A. I. Barakat, "Vascular endothelial wound closure under shear stress: Role of membrane fluidity and flow-sensitive ion channels," *J Appl Physiol (1985)*, vol. 98, no. 6, pp. 2355–62, 2005, ISSN: 8750-7587 (Print) 0161-7567 (Linking). DOI: 10.1152/japplphysiol.01136.2004. [Online]. Available: https://www.ncbi.nlm.nih.gov/pubmed/15705727.

[14] S. Kasas, A. Kis, B. M. Riederer, L. Forro, G. Dietler, and S. Catsicas, "Mechanical properties of microtubules explored using the finite elements method," *Chemphyschem*, vol. 5, no. 2, pp. 252–7, 2004, ISSN: 1439-4235 (Print) 1439-4235 (Linking). DOI: 10.1002/cphc.200300799. [Online]. Available: https://www.ncbi.nlm.nih.gov/pubmed/15038290.

[15] C. P. Brangwynne, F. C. MacKintosh, S. Kumar, *et al.*, "Microtubules can bear enhanced compressive loads in living cells because of lateral reinforcement," *J Cell Biol*, vol. 173, no. 5, pp. 733–41, 2006, ISSN: 0021-9525 (Print) 0021-9525 (Linking). DOI: 10.1083/jcb.200601060. [Online]. Available: https://www.ncbi.nlm.nih.gov/pubmed/16754957.

[16] J. B. Manneville, S. Etienne-Manneville, P. Skehel, T. Carter, D. Ogden, and M. Ferenczi, "Interaction of the actin cytoskeleton with microtubules regulates secretory organelle movement near the plasma membrane in human endothelial cells," *J Cell Sci*, vol. 116, no. Pt 19, pp. 3927–38, 2003, ISSN: 0021-9533 (Print) 0021-9533 (Linking). DOI: 10.1242/jcs.00672. [Online]. Available: https://www.ncbi.nlm.nih.gov/pubmed/12928328.

[17] A. L. Hazel and T. J. Pedley, "Vascular endothelial cells minimize the total force on their nuclei," *Biophys J*, vol. 78, no. 1, pp. 47–54, 2000, ISSN: 0006-3495 (Print) 0006-3495 (Linking). DOI: 10.1016/S0006-3495(00)76571-4. [Online]. Available: https://www.ncbi.nlm.nih.gov/pubmed/10620272.

[18] J. L. Broers, F. C. Ramaekers, G. Bonne, R. B. Yaou, and C. J. Hutchison, "Nuclear lamins: Laminopathies and their role in premature ageing," *Physiol Rev*, vol. 86, no. 3, pp. 967–1008, 2006, ISSN: 0031-9333 (Print) 0031-9333 (Linking). DOI: 10.1152/physrev.00047.2005. [Online]. Available: https://www.ncbi.nlm.nih.gov/pubmed/16816143.

[19] E. A. Booth, S. T. Spagnol, T. A. Alcoser, and K. N. Dahl, "Nuclear stiffening and chromatin softening with progerin expression leads to an attenuated nuclear response to force," *Soft Matter*, vol. 11, no. 32, pp. 6412–8, 2015, ISSN: 1744-6848 (Electronic) 1744-683X (Linking). DOI: 10.1039/c5sm00521c. [Online]. Available: https://www.ncbi.nlm.nih.gov/pubmed/26171741.

[20] X. Wang, R. Bleher, M. E. Brown, *et al.*, "Nano-biomechanical study of spatio-temporal cytoskeleton rearrangements that determine subcellular mechanical properties and endothelial permeability," *Sci Rep*, vol. 5, p. 11 097, 2015, ISSN: 2045-2322 (Electronic) 2045-2322 (Linking). DOI: 10.1038/srep11097. [Online]. Available: https://www.ncbi.nlm.nih.gov/pubmed/26086333.

[21] R. Varga, M. Eriksson, M. R. Erdos, *et al.*, "Progressive vascular smooth muscle cell defects in a mouse model of hutchinson-gilford progeria syndrome," *Proc Natl Acad Sci U S A*, vol. 103, no. 9, pp. 3250–5, 2006, ISSN: 0027-8424 (Print) 0027-8424 (Linking). DOI: 10.1073/pnas.0600012103. [Online]. Available: https://www.ncbi.nlm.nih.gov/pubmed/16492728.

[22] V. Andres and J. M. Gonzalez, "Role of a-type lamins in signaling, transcription, and chromatin organization," *J Cell Biol*, vol. 187, no. 7, pp. 945–57, 2009, ISSN: 1540-8140 (Electronic) 0021-9525 (Linking). DOI: 10.1083/jcb.200904124. [Online]. Available: https://www.ncbi.nlm.nih.gov/pubmed/20038676.

[23] P. Scaffidi and T. Misteli, "Lamin a-dependent nuclear defects in human aging," *Science*, vol. 312, no. 5776, pp. 1059–63, 2006, ISSN: 1095-9203 (Electronic) 0036-8075 (Linking). DOI: 10.1126/science.1127168. [Online]. Available: https://www.ncbi.nlm.nih.gov/pubmed/16645051.

[24] J. A. Brassard, N. Fekete, A. Garnier, and C. A. Hoesli, "Hutchinson-gilford progeria syndrome as a model for vascular aging," *Biogerontology*, vol. 17, no. 1, pp. 129–45, 2016, ISSN: 1573-6768 (Electronic) 1389-5729 (Linking). DOI: 10.1007/s10522-015-9602-z. [Online]. Available: https://www.ncbi.nlm.nih.gov/pubmed/26330290.

[25] M. Olive, I. Harten, R. Mitchell, *et al.*, "Cardiovascular pathology in hutchinson-gilford progeria: Correlation with the vascular pathology of aging," *Arterioscler Thromb Vasc Biol*, vol. 30, no. 11, pp. 2301–9, 2010, ISSN: 1524-4636 (Electronic) 1079-5642 (Linking). DOI: 10.1161/ATVBAHA.110.209460. [Online]. Available: https://www.ncbi.nlm.nih.gov/pubmed/20798379.

[26] J. G. McGarry and P. J. Prendergast, "A three-dimensional finite element model of an adherent eukaryotic cell," *Eur Cell Mater*, vol. 7, 27–33, discussion 33–4, 2004, ISSN: 1473-2262 (Electronic) 1473-2262 (Linking). DOI: 10.22203/ecm.v007a03. [Online]. Available: https://www.ncbi.nlm.nih.gov/pubmed/15095253.

[27] L. Chua, "Finite element modelling of living cells," Thesis, 2014.

[28] Y. Ujihara, M. Nakamura, H. Miyazaki, and S. Wada, "Proposed spring network cell model based on a minimum energy concept," *Ann Biomed Eng*, vol. 38, no. 4, pp. 1530–8, 2010, ISSN: 1573-9686 (Electronic) 0090-6964 (Linking). DOI: 10.1007/s10439-010-9930-8. [Online]. Available: https://www.ncbi.nlm.nih.gov/pubmed/20108165.

[29] H. Karcher, J. Lammerding, H. Huang, R. T. Lee, R. D. Kamm, and M. R. Kaazempur-Mofrad, "A three-dimensional viscoelastic model for cell deformation with experimental verification," *Biophys J*, vol. 85, no. 5, pp. 3336–49, 2003, ISSN: 0006-3495 (Print) 0006-3495 (Linking). DOI: 10.1016/S0006-3495(03)74753-5. [Online]. Available: https://www.ncbi.nlm.nih.gov/pubmed/14581235.

[30] V. Jakka and J. Bursa, "Finite element simulations of mechanical behaviour of endothelial cells," *Biomed Res Int*, vol. 2021, p. 8 847 372, 2021, ISSN: 2314-6141 (Electronic). DOI: 10.1155/2021/8847372. [Online]. Available: https://www.ncbi.nlm.nih.gov/pubmed/33681382.

[31] M. L. Gardel, K. E. Kasza, C. P. Brangwynne, J. Liu, and D. A. Weitz, "Chapter 19: Mechanical response of cytoskeletal networks," *Methods Cell Biol*, vol. 89, pp. 487–519, 2008, ISSN: 0091-679X (Print) 0091-679X (Linking). DOI: 10.1016/S0091-679X(08)00619-5. [Online]. Available: https://www.ncbi.nlm.nih.gov/pubmed/19118688.

[32] J. S. Palmer and M. C. Boyce, "Constitutive modeling of the stress-strain behavior of f-actin filament networks," *Acta Biomater*, vol. 4, no. 3, pp. 597–612, 2008, ISSN: 1742-7061 (Print) 1742-7061 (Linking). DOI: 10.1016/j.actbio.2007.12.007. [Online]. Available: https://www.ncbi.nlm.nih.gov/pubmed/18325860.

[33] C. Poon, "Measuring the density and viscosity of culture media for optimized computational fluid dynamics analysis of in vitro devices," Aug. 2020. DOI: 10.1101/2020.08.25.266221.

[34] P. F. Davies, T. Mundel, and K. A. Barbee, "A mechanism for heterogeneous endothelial responses to flow in vivo and in vitro," *Journal of Biomechanics*, vol. 28, no. 12, pp. 1553–1560, 1995, ISSN: 0021-9290 (Electronic) 0021-9290 (Linking). DOI: 10.1016/0021-9290(95)00102-6. [Online]. Available: https://pubmed.ncbi.nlm.nih.gov/8666594/.

[35] T. Al-Muhtaseb, "Building a tensegrity-based computational model to understand endothelial alignment under flow," M.S. thesis, Purdue University, 2021. [Online]. Available: https://hammer.purdue.edu/articles/thesis/Building_A_Tensegrity-Based_Computational_Model_to_Understand_Endothelial_Alignment_Under_Flow/16791436.